Research Square

Preprints are preliminary reports that have not undergone peer review.
They should not be considered conclusive, used to inform clinical practice,
or referenced by the media as validated information.

Mitochondrial DNA-cGAS-STING-CISD1 axis mediates hypoxia-induced cognitive impairment by driving hippocampal neuronal ferroptosis

Qian Chen
Xizang Minzu University
Handan Zheng
Xizang Minzu University
Xiaokang Hao
Affiliated Hospital of Xizang Minzu University
Yujie Feng
Xizang Minzu University
Yiyi Zhu
Xizang Minzu University
Hang Liu
Xizang Minzu University
Zhang Jie
Xizang Minzu University
Yuxing Li
Xizang Minzu University
Jiaqi Li
Xizang Minzu University
Shucheng Qiao
Xizang Minzu University
Hui Ma
Xizang Minzu University
Chaoren Yan
Xizang Minzu University
Ying Zheng
Xizang Minzu University
Jingming Shi
shijingming5272@126.com

Xizang Minzu University

Research Article

Keywords: Hypoxia, Cognitive impairment, Ferroptosis, cGAS-STING signaling pathway

Posted Date: November 2nd, 2026

DOI: https://doi.org/10.21203/rs.3.rs-11392101/v1

License: This work is licensed under a Creative Commons Attribution 4.0 International License.
Read Full License

Additional Declarations: No competing interests reported.

Abstract

High-altitude hypoxic cognitive impairment severely compromises the physical and mental health of individuals who rapidly ascend to or reside long-term at high altitude; however, its initiating mechanisms, pathological cascades, and molecular regulatory network remain incompletely understood, leaving a paucity of effective therapeutic targets and preventive strategies. Using a mouse model of simulated 6000 m hypobaric hypoxia and a primary hippocampal neuron hypoxia model, we integrated behavioral testing, transmission electron microscopy, Seahorse metabolic analysis, transcriptomic profiling, co-immunoprecipitation-coupled proteomics, structural prediction, pharmacological intervention, and clinical validation in human cohorts to systematically delineate the molecular mechanisms and core regulatory pathways underlying hypoxia-induced neuronal ferroptosis. Hypoxic exposure time-dependently impaired object recognition and spatial memory in mice and caused hippocampal neuron loss. Mechanistically, mitochondrial damage emerged as a critical initiating event during hypoxic stress, triggering mitochondrial DNA (mtDNA) release and subsequent activation of the cGAS-STING signaling pathway. Hypoxic hippocampal neurons exhibited canonical features of ferroptosis, including elevated Fe^{2+} and malondialdehyde (MDA) levels, decreased GPX4 expression, and enhanced ACSL4 expression and increased mitochondrial C11-BODIPY oxidation. Pharmacological inhibition of STING with C-176 significantly alleviated these ferroptosis phenotypes, neuronal loss, and cognitive impairment. Co-immunoprecipitation combined with proteomics identified CISD1 (mitoNEET), a mitochondrial outer membrane protein, as a STING-interacting partner, and their binding was enhanced under hypoxia and localized to mitochondria-endoplasmic reticulum contact sites. Moreover, the ferroptosis inhibitor Liproxstatin-1 rescued hypoxic cognitive impairment and partially restored mitochondrial morphology and respiratory function without reversing STING phosphorylation, indicating that ferroptosis functions downstream of STING and constitutes a feed-forward amplification loop by aggravating mitochondrial damage. In human cohorts, levels of serum iron and oxidative damage markers correlated positively with residential altitude. Collectively, these findings establish a self-amplifying pathological axis of mitochondrial damage-mtDNA-cGAS-STING-CISD1-ferroptosis, and targeting this axis may provide novel strategies for the prevention and treatment of high-altitude hypoxic cognitive impairment.

1. Introduction

Approximately 81 million people worldwide reside permanently at altitudes above 2,500 m, and tens of millions of individuals rapidly ascending to high altitudes each year also face sustained hypobaric hypoxia exposure. Epidemiological and cohort studies have consistently demonstrated that high-altitude exposure causes cognitive decline, primarily characterized by impairments in learning and memory, attention, and executive function, frequently accompanied by anxiety, depression, and sleep disturbances, which significantly affect occupational performance and long-term health[1–3]. The hippocampus is one of the brain regions most sensitive to hypoxia, and neuronal loss in this area is considered the structural basis of cognitive impairment. However, the initiating events of hypoxia-induced hippocampal neuronal death, the specific form of regulated cell death involved, and the

intracellular signaling pathways that amplify this process remain poorly understood, which has directly precluded the identification of effective targeted preventive and therapeutic strategies in clinical practice[4–6]. Therefore, cognitive impairment induced by high-altitude hypoxia has emerged as a critical challenge in high-altitude medicine that requires urgent attention.

Ferroptosis is a form of regulated cell death driven by iron-dependent lipid peroxidation[7], characterized by the failure of the GPX4-GSH antioxidant system, ACSL4-mediated phospholipid remodeling with polyunsaturated fatty acids, and accumulation of free ferrous iron[8]. The central nervous system (CNS), which is rich in polyunsaturated fatty acids with high oxygen consumption and limited antioxidant reserves, rendering it particularly susceptible to iron homeostasis dysregulation; Ferroptosis has been implicated in the pathogenesis of cerebral ischemia-reperfusion injury, neurodegenerative diseases, and traumatic brain injury[9–11]. Hypoxic environments can simultaneously provide two potential prerequisites for ferroptosis: increased generation of mitochondria-derived reactive oxygen species (ROS) and HIF-mediated iron metabolism remodeling. Nevertheless, definitive in vivo interventional evidence regarding whether ferroptosis is activated in high-altitude hypobaric hypoxia-induced cognitive impairment and whether it causally contributes to neuronal loss remains lacking.

Mitochondria serve as the primary sites of cellular energy metabolism and ROS production. Under hypoxic stress, the electron transport chain is constrained, oxidative phosphorylation efficiency declines, and ROS generation increases[12], which may ultimately lead to disruption of mitochondrial cristae architecture and alteration of mitochondrial membrane permeability, thereby causing mtDNA release into the cytosol[13]. Cytosolic mtDNA, acting as a damage-associated molecular pattern, is recognized by the cytosolic DNA sensor cyclic GMP-AMP synthase (cGAS), thereby activating it; Activated cGAS catalyzes the production of the second messenger 2'3'-cGAMP, which binds to and activates the adaptor protein STING (Stimulator of Interferon Genes); STING subsequently recruits the kinase TBK1, which in turn phosphorylates the transcription factor IRF3, inducing type I interferon expression and NF-κB-mediated inflammatory responses. This pathway has been demonstrated to participate not only in antiviral innate immunity but also in sterile inflammation, mitochondria damage-associated inflammation, and the pathogenesis of various chronic diseases[14,15]. However, the cGAS-STING pathway has long been considered to be mainly carried by microglia in the CNS. Direct evidence is lacking as to whether neurons themselves can undergo cell-autonomous STING activation in response to hypoxic stimulation and thereby dictate their survival. More importantly, the downstream effects of the STING pathway have previously been almost exclusively attributed to interferon and inflammatory outputs; whether it can directly regulate ferroptosis, a non-inflammatory cell death program, remains unclear.

CISD1 (CDGSH iron-sulfur domain-containing protein 1, also known as mitoNEET) is an iron-sulfur cluster-binding protein localized on the outer mitochondrial membrane[16], which participates in mitochondrial iron distribution, redox homeostasis, and respiratory chain assembly by transferring iron-sulfur clusters to acceptor proteins[17]. Previous studies have shown that CISD1 can limit mitochondrial lipid peroxidation and protect against ferroptosis, while its knockdown sensitizes cells to ferroptosis

inducers[18]. However, under pathological stress conditions such as LPS-induced acute lung injury[19], gastric cancer[20], and neurodegenerative diseases[21], upregulated CISD1 expression is associated with exacerbated tissue and cellular injury and poor prognosis, suggesting that CISD1 is not an exclusively protective molecule. Its biological function can be modulated by post-translational modifications, protein-protein interactions, and microenvironmental signals, thereby enabling a functional switch. Notably, activated STING undergoes trafficking along the endoplasmic reticulum-Golgi pathway[22]. Mitochondria-associated endoplasmic reticulum membranes (MAMs), which are membrane contact sites between the endoplasmic reticulum and the outer mitochondrial membrane, are considered potential checkpoints regulating STING trafficking[23]. CISD1 is localized on the outer mitochondrial membrane, a region precisely at the physical interface of MAM[24], providing spatial possibility for their interaction. However, no experimental studies have yet tested this hypothesis.

Therefore, this study aims to establish causal relationships and define hierarchical mechanisms by employing *in vivo* and *in vitro* models, pharmacological interventions, and multi-omics analyses. It will also elucidate the STING-CISD1 interaction using co-immunoprecipitation and structural prediction, and finally evaluate the translational value of relevant biomarkers in a high-altitude population cohort. Overall, this study will systematically dissect the mechanistic chain linking hypoxia-induced mitochondrial damage, innate immune activation, and ferroptosis, potentially providing a new theoretical foundation and therapeutic targets for interventions for high-altitude hypoxia-related neurological injury.

2. Materials and Methods

2.1 Animals

Male C57BL/6 mice (approximately 8 weeks old) were purchased from Chengdu Dossy Experimental Animals Co., Ltd. (Chengdu, China) and housed in a specific-pathogen-free (SPF) animal facility under controlled temperature (25 ± 2℃) and humidity (50–60%) with a 12-h light/12-h dark cycle. Food and water were provided *ad libitum*. After 7 days of acclimatization, mice were randomly assigned to the normoxia group, hypoxia groups (3, 5, and 7 days), and corresponding drug intervention groups. Hypoxia exposure was performed in a hypobaric hypoxia chamber (ProOx-811; Shanghai Tawang Intelligent Technology Co., Ltd., Shanghai, China) to simulate a high-altitude environment at 6000 m. The ascent and descent phases each lasted 30 min, and mice were maintained under hypoxic conditions for 3, 5, or 7 days, respectively. During hypoxia exposure, mice were monitored daily at scheduled time points for any signs of pain or distress, including self-mutilation, loss of locomotion, altered breathing patterns, abnormal posture, urine and fecal quality, tremor, or convulsions. For drug intervention experiments, mice received intraperitoneal injections of Liproxstatin-1 or C-176 (10 mg/kg) at a fixed time daily for 7 consecutive days during hypoxia exposure; control mice received an equal volume of vehicle. After completion of behavioral tests, mice were anesthetized by intraperitoneal injection of sodium pentobarbital and euthanized for tissue collection. Hippocampal tissues were rapidly dissected and stored at − 80℃ for protein, RNA, and biochemical analyses. The remaining mice were transcardially

perfused, and various brain regions were collected and fixed in 4% paraformaldehyde for subsequent immunofluorescence and histological staining. All animal experiments were conducted in strict accordance with the guidelines of the Biomedical Ethics Committee of Xizang Minzu University (approval no. 2026-03-003) and complied with the 3R principles (Replacement, Reduction, Refinement) and animal welfare requirements.

2.2 Behavioral Tests

Behavioral tests included the Novel Object Recognition (NOR) test to assess recognition memory; the Morris water maze test, comprising place navigation training and spatial probe trials, to evaluate spatial learning and memory; the Nest Building Test to assess daily living ability, motivational state, and integration of complex behaviors; and the T-maze test to evaluate working memory. Prior to testing, mice were acclimated to the behavioral laboratory, and all behavioral tests were conducted in a quiet environment with stable lighting. Behavioral trajectories and related parameters were recorded and visualized using the SMART animal behavior tracking and analysis system (Shenzhen Reward Life Technology Co., Ltd., Shenzhen, China). All behavioral tests were performed by investigators blinded to group assignment to minimize subjective bias as much as possible.

2.3 Primary Neuron Culture and Hypoxia Treatment

Primary neurons were isolated from neonatal C57BL/6 mouse pups within 24 h of birth. Normoxic culture conditions were maintained at 37℃ in a humidified atmosphere of 5% CO_2 and 95% air. Hypoxic conditions were set at 37°C in a tri-gas incubator with 5% CO_2, 1% O_2, and 94% N_2. Briefly, brains were dissected from C57BL/6 pups after ethanol disinfection and placed in DMEM containing penicillin-streptomycin. Hippocampi were carefully isolated under a dissecting microscope and transferred to 1.5-mL centrifuge tubes. Tissues were digested with 1 mL of 0.25% trypsin in a 37℃ water bath for 15 min, followed by addition of serum-containing medium to terminate digestion. Dissociated cells were triturated into a single-cell suspension and seeded onto poly-D-lysine (PDL)-coated culture plates in medium supplemented with penicillin/streptomycin (100 U/mL each). Neurons cultured for 14 days were used for subsequent experiments.

2.4 Nissl Staining and Hematoxylin-Eosin(HE) Staining of Brain Tissue

Perfused and fixed whole brains were dehydrated through a graded ethanol series, cleared in xylene, and embedded in paraffin. Serial coronal sections (4 μm thick) were mounted on glass slides and baked at 60°C for 2 h prior to staining. HE staining was performed using a commercial kit (Servicebio, Wuhan, China) according to the manufacturer's instructions. Briefly, sections were deparaffinized in xylene, rehydrated through a graded ethanol series, and sequentially stained with hematoxylin for nuclei, differentiated, blued in running water, and counterstained with eosin. Sections were then dehydrated through graded ethanol, cleared in xylene, and mounted with neutral balsam. Nissl staining was performed using a commercial kit (Biosharp, Anhui, China) according to the manufacturer's protocol. Briefly, after deparaffinization and rehydration, sections were stained with toluidine blue working solution,

dehydrated through graded ethanol, cleared in xylene, and mounted with neutral balsam. Representative images of the entire hippocampus and its CA1, CA2, CA3, and dentate gyrus (DG) subregions were captured using a light microscope. For each mouse, three consecutive sections at approximately the same anatomical level were randomly selected for staining and observation. An investigator blinded to group assignment performed image analysis using ImageJ software (National Institutes of Health, Bethesda, MD, USA). For HE staining, neurons with intact soma, clear nuclei, and regular arrangement were counted as surviving neurons. For Nissl staining, neurons with intact soma, clear nuclear structure, and distinct Nissl bodies in the cytoplasm were counted as positive cells. Results are expressed as the number of neurons per unit area (cells/mm²).

2.5 Immunofluorescence Staining

Tissue preparation: Perfused and fixed whole brains were dehydrated in 10%, 20%, and 30% sucrose solutions until the tissues were fully submerged. Brains were then embedded in OCT compound and serially sectioned in the coronal plane (25 μm thick) using a cryostat. Sections were mounted on glass slides and stored at 4°C in a humidified chamber until use. Cell preparation: Primary neurons were seeded onto sterile coverslips placed in 24-well culture plates. Following maturation and specific treatments, the culture medium was aspirated, and cells were gently washed with pre-chilled PBS before being fixed with 4% paraformaldehyde for 15 min at room temperature. Subsequent steps were identical for both tissues and cells: permeabilization with 0.3% Triton X-100 for 15 min at room temperature, blocking for 2 h at room temperature, and incubation with primary antibodies overnight at 4°C in the dark. Primary antibodies used were as follows: MAP2 (Abmart, 1:2000), NeuN (Abmart, 1:5000), dsDNA (Sigma, 1:8000), phosphorylated STING (p-STING, Abmart, 1:5000), and CISD1 (Proteintech, 1:2000). On the following day, samples were brought to room temperature, washed three times with PBS, and incubated with Alexa Fluor 594-conjugated goat anti-rabbit IgG secondary antibody (Abmart, 1:8000) for 2 h at room temperature in the dark. After incubation, samples were washed with PBS and mounted with anti-fade mounting medium containing DAPI. All fluorescence images were acquired using a laser confocal microscope (Leica TCS SP8). Images for all samples were acquired under identical laser power, gain, exposure time, and acquisition parameters. For each mouse, three consecutive sections at the same anatomical level were randomly selected, and images of the hippocampal CA1, CA2, CA3, and DG regions were captured. Fluorescence intensity and positive signals were quantified using ImageJ software by an investigator blinded to group assignment.

2.6 Western Blot

Appropriate amounts of tissue or cell samples were lysed thoroughly in a pre-chilled homogenizer with RIPA lysis buffer containing protease and phosphatase inhibitors. The lysates were then centrifuged at 4℃ and 12,000×g for 15 min, and the supernatants were collected as total protein samples. Protein concentrations were determined using a BCA protein quantification kit. The protein extracts were mixed with loading buffer and denatured at 95℃ for 10 min in a heating block. Proteins were separated via SDS-PAGE, transferred onto PVDF membranes, and blocked with 5% BSA at room temperature for 2 h, followed by overnight incubation at 4℃ with the following primary antibodies: HIF1α (Abmart, 1:3000),

GPX4 (Abmart, 1:6000), XCT (Abmart, 1:5000), ACSL4 (Abclone, 1:2500), TOMM20 (Proteintech, 1:5000), FTH1 (Immunoway, 1:3500), cGAS (Proteintech, 1:2500), STING (Abmart, 1:3000), p-STING (Abmart, 1:3000), TBK1 (Immunoway, 1:3000), p-TBK1 (Immunoway, 1:2500), IRF3 (Proteintech, 1:5000), p-IRF3 (Abmart, 1:2500), CISD1 (Proteintech, 1:2500), and β-actin (Biosharp, 1:8000). Following primary antibody incubation, the membranes were washed three times with TBST, incubated with an HRP-conjugated universal secondary antibody (Abmart, 1:10000) at room temperature in the dark for 2 h, and washed again. Bands were visualized using an enhanced chemiluminescent reagent and captured with a chemiluminescence imaging system. Band gray values were quantified using ImageJ software. Non-phosphorylated target protein expression was normalized to the internal reference β-actin, while phosphorylated protein levels were normalized to their corresponding total proteins; these quantitative results were used for subsequent statistical analysis. Information on all antibodies used in this study was provided in supplementary Table 1.

2.7 RT-qPCR

Appropriate amounts of mouse hippocampal tissue or cell samples were thoroughly lysed with 1 ml of TRIGene Plus total RNA extraction reagent (GenStar, Cat#P108-05, Beijing, China). Total RNA was obtained through sequential extraction, precipitation, and washing steps. RNA concentration and purity were measured using a NanoDrop microspectrophotometer (Thermo Fisher Scientific, Waltham, MA, USA). High-quality RNA samples underwent reverse transcription using the StarScript III RT SuperMix for qPCR (with gDNA Remover) (GenStar, Cat#A241-10, Beijing, China) according to the manufacturer's protocol to eliminate genomic DNA contamination and synthesize first-strand cDNA. Amplification and data collection were performed using the Bio-Rad CFX96 Connect real-time quantitative PCR system (Bio-Rad Laboratories, Hercules, CA, USA). Target genes were detected using the SYBR Green fluorescence mode, with β-actin serving as the internal reference gene for normalization. Relative mRNA expression levels were calculated using the 2^−ΔΔCt method. Specific primer sequences and detailed information of reagents used in this study were provided in the supplementary Table 2–3.

2.8 Transmission Electron Microscopy (TEM)

After respective treatments, the culture medium was removed from primary neurons in each group, and cells were gently washed with pre-chilled PBS. Cells were fixed with pre-chilled electron microscopy fixative (Servicebio, Cat#G1102), gently resuspended by trituration to collect cell suspensions, and transferred to centrifuge tubes for low-speed centrifugation to form cell pellets. Pellets were then fixed in 2.5% glutaraldehyde overnight at 4℃. Fixed samples were rinsed with 0.1 mol/L phosphate buffer and post-fixed with 1% osmium tetroxide for 1–2 h at room temperature. Samples were then dehydrated through a graded ethanol series (30%, 50%, 70%, 80%, 90%, 95%, and 100%), each for 10–15 min, followed by acetone substitution, infiltration, and embedding in epoxy resin. Embedded samples were polymerized and cured, and ultrathin sections (60–80 nm) were cut using an ultramicrotome and collected on copper grids. Ultrathin sections were double-stained with uranyl acetate and lead citrate, and images were acquired using a transmission electron microscope. Multiple independent fields were randomly selected for each group, with particular attention to mitochondrial membrane structure, cristae

architecture, electron density, swelling, vacuolization, and morphological integrity. Mitochondrial morphology was assessed using ImageJ software, with quantitative parameters including mitochondrial perimeter, area, and aspect ratio.

2.9 Seahorse Cellular Energy Metabolism Analysis

The Seahorse XFe 24 Extracellular Flux Analyzer (Agilent Technologies) was used to measure the oxygen consumption rate (OCR) of cells in each group. Mitochondrial electron transport chain (ETC) inhibitors were sequentially injected: oligomycin (ATP synthase inhibitor, 1.5 μM), FCCP (mitochondrial uncoupler, 1.5 μM), and rotenone/antimycin A (complex I and III inhibitors, 0.5 μM). Key parameters reflecting mitochondrial function were calculated, including basal respiration, ATP-linked respiration, proton leak, maximal respiration, spare respiratory capacity, and non-mitochondrial oxygen consumption. OCR was recorded in real time and automatically analyzed using Wave software (n = 4 per group); subsequently, intergroup comparisons were performed.

2.10 RNA-Seq and Bioinformatic Analysis

Primary neurons were exposed to normoxia or hypoxia for 24 h, and samples were sent to Shanghai Majorbio Bio-Pharm Technology Co., Ltd. for RNA sequencing (n = 3 biological replicates per group). Library construction involved total RNA extraction, mRNA isolation and fragmentation, first- and second-strand cDNA synthesis, end repair of double-stranded cDNA, adapter ligation, and PCR enrichment. Subsequently, bioinformatic analyses including principal component analysis (PCA), Pearson correlation, volcano plots of differentially expressed genes, Gene Ontology (GO) enrichment analysis, and Kyoto Encyclopedia of Genes and Genomes (KEGG) enrichment analysis were performed to compare the two groups.

2.11 Co-Immunoprecipitation–Proteomic Analysis

Hippocampal tissues and primary neurons from the hypoxia group were lysed on ice in pre-chilled IP lysis buffer supplemented with protease and phosphatase inhibitors. After thorough lysis, samples were centrifuged at 12,000 × g for 15 min at 4°C, and the supernatant was collected as total protein lysate. The STING-specific antibody and the isotype IgG negative control antibody were each diluted at 1:100 and incubated with pre-washed Protein A/G magnetic beads (MCE, HY-K0202) overnight at 4°C with slow rotation. The next day, unbound antibody was removed, and beads were gently washed three times with PBST. Equal amounts of total protein (approximately 1.5 mg) from each group were then added and incubated overnight at 4°C with rotation to allow antigen–antibody complexes to bind to the beads. After incubation, beads were gently and thoroughly washed five times with PBST to remove non-specifically bound proteins. One portion of the immunoprecipitated samples was sent directly to Shanghai Majorbio Bio-Pharm Technology Co., Ltd. for high-throughput global proteomic analysis. The remaining portion was eluted by adding 5× protein loading buffer to the beads and heating at 95°C for 10 min; eluted products were collected for subsequent Western blot analysis. Input samples were used to confirm total expression levels of target proteins; the IgG group served as a negative control; and the IP group was used to evaluate the interaction between CISD1 (Proteintech, 1:2500) and STING (Abmart, 1:3000). A

universal light-chain-specific secondary antibody (Abmart, 1:2500) was used to avoid interference from antibody heavy and light chains. Band intensity was quantified using ImageJ software. CISD1 signals were normalized to immunoprecipitated STING signals for intergroup comparison.

2.12 Molecular Docking, Database Intersection, and PPI Network

High-throughput Co-IP proteomic datasets from hippocampal tissues and primary neurons were cross-referenced to identify overlapping proteins, which were then compared against ferroptosis-related genes derived from the FerrDb database (http://www.zhounan.org/ferrdb), including ferroptosis drivers, suppressors, and markers, using Venn analysis. A total of 9 key candidate ferroptosis-related genes that interact with STING were identified. Candidate genes were imported into the STRING database (https://string-db.org) to construct a protein–protein interaction (PPI) network. The species was limited to *Mus musculus*, and the minimum required interaction score was set at 0.400. Key candidate proteins were screened based on topological parameters such as node degree, and the network was visualized. Subsequently, protein–protein molecular docking analysis was performed between key candidate proteins and STING. The three-dimensional structure of STING was downloaded from the Protein Data Bank (PDB ID: 4LOJ), and the structure of CISD1 was obtained from the AlphaFold Protein Structure Database (AlphaFold ID: AF-Q91WS0-F1). Before docking, water molecules and ligands were removed from the protein structures, polar hydrogen atoms were added, and structures were saved in PDB format. Protein–protein molecular docking was performed using the HDOCK Server (http://hdock.phys.hust.edu.cn/) with global rigid docking under default parameters. Resulting conformations were ranked according to the HDOCK docking score, and the model with the highest score and a reasonable binding interface was selected as the optimal binding conformation. The protein binding interface and interacting residues were analyzed using PDBePISA (Protein Interfaces, Surfaces and Assemblies), and hydrogen bonds and interface contact residues were documented. The optimal docking conformation and interaction interface were visualized using PyMOL.

2.13 Clinical Cohort and Related Biomarker Measurements

Peripheral venous blood samples and corresponding clinical data were collected from first-year college students undergoing physical examination at the Medical Examination Center of the Affiliated Hospital of Xizang Minzu University. Written informed consent was obtained from all participants. The study protocol was approved by the Ethics Committee of Xizang Minzu University and conducted in strict accordance with the ethical principles of the Declaration of Helsinki for human research. Based on their long-term residential altitude, participants were initially stratified into a low-altitude group (< 2500 m) and a high-altitude group (≥ 2500 m) to compare clinical biochemical parameters between these populations. Fasting peripheral venous blood samples were collected, and biochemical parameters were measured by the clinical laboratory center according to standardized hospital protocols. Measured parameters included: (1) Liver function indicators: total protein (TP), albumin (ALB), globulin (GLB), albumin/globulin ratio (A/G), total bilirubin (TBIL), direct bilirubin (DBIL), indirect bilirubin (IBIL), total bile acid (TBA), alkaline phosphatase (ALP), γ-glutamyl transpeptidase (GGT), alanine aminotransferase (ALT), and

aspartate aminotransferase (AST); (2) Lipid metabolism indicators: low-density lipoprotein cholesterol (LDL-C), total cholesterol (TC), triglycerides (TG), apolipoprotein A1 (ApoA1), high-density lipoprotein cholesterol (HDL-C), apolipoprotein A/B ratio (ApoA/B), and apolipoprotein B (ApoB); (3) Inflammatory indicators: high-sensitivity C-reactive protein (hs-CRP) and interleukin-6 (IL-6). All measurements were performed using an automated biochemical analyzer with matched reagents; the instrument was calibrated and subjected to quality control procedures in accordance with the hospital's unified quality control system. In addition, to further investigate the broad potential effects of altitude gradient changes on systemic metabolism, participants meeting the inclusion criteria were stratified by altitude gradient (≤ 1500 m, 1500–3500 m, and ≥ 3500 m), and collected serum samples were subjected to proteomic sequencing analysis.

2.14 Statistical Analysis

All quantitative data were expressed as the mean ± standard error of the mean (SEM), and statistical analyses were performed using GraphPad Prism 10.0 software. Prior to statistical analysis, the Shapiro–Wilk test was used to assess normality, and the Brown–Forsythe test and Bartlett's test were used to evaluate homogeneity of variances among groups. Parametric tests were used when data were normally distributed with homogeneous variances; otherwise, corresponding non-parametric tests or variance-corrected methods were applied. All statistical tests were two-tailed, and $P < 0.05$ was considered statistically significant. For comparisons between two independent groups (e.g., histological staining, immunofluorescence, RT-qPCR, and Western blot results between normoxia and hypoxia groups), an unpaired two-tailed *t*-test was used when data were normally distributed; Welch's correction was applied when variances were unequal. For comparisons among three or more independent groups (e.g., behavioral, molecular, and mitochondrial functional parameters among different hypoxia duration groups, hypoxia plus LIP-1 group, hypoxia plus C-176 group, and corresponding control groups), ordinary one-way ANOVA was used when data were normally distributed with homogeneous variances. Tukey's post hoc multiple comparison test was used for pairwise comparisons among all groups when appropriate. Specific statistical methods are detailed in each figure legend.

3. Results

3.1 Hypoxia exposure induces cognitive impairment in mice

To investigate the pathological mechanisms underlying high-altitude hypoxic cognitive impairment, we established an animal model using a hypobaric hypoxia chamber to simulate a high-altitude environment (6000 m; 3, 5, and 7 days of exposure). Behavioural testing and tissue collection were performed at the corresponding time points as illustrated (Fig. 1A). Compared with normoxic controls, hypoxia-exposed mice showed a progressive reduction in body weight that became more pronounced with prolonged exposure, accompanied by a significant decrease in brain weight (Fig. 1B). We next evaluated brain function using a battery of behavioural tests. Behavioral assessment revealed: Excluding differences in

motor ability (Supplementary Fig. S1, swimming speed and total exploration distance did not differ significantly between groups), in the novel object recognition (NOR) test, the distance, time, and exploration-frequency indices were all significantly reduced in hypoxia-exposed mice, with the most pronounced deficits observed in the 7-day group (Fig. 1C). In the Morris water maze (MWM), representative swim trajectories indicated diminished search behaviour within the target quadrant, and the number of platform crossings, the percentage of swimming distance in the target quadrant, and the percentage of time spent in the target quadrant were all significantly decreased, with deficits worsening as the duration of exposure increased (Fig. 1D). Nesting scores did not differ between the 3-day hypoxia group and normoxic controls, whereas mice exposed to hypoxia for 5 and 7 days exhibited markedly looser and less integrated nests with significantly reduced nesting scores (Fig. 1E). In the T-maze test, correct-choice rate was significantly reduced only in the 7-day hypoxia group (Fig. 1F). Collectively, these results demonstrate that prolonged hypoxia induces body and brain weight loss together with multidimensional cognitive deficits spanning recognition, spatial, and working memory, with several parameters deteriorating in a time-dependent manner. Accordingly, 7 days of hypoxia exposure was selected as the principal modelling time point for subsequent mechanistic studies.

3.2 Hypoxia induces hippocampal neuronal damage and ferroptosis-associated molecular alterations

Given the pronounced cognitive deficits induced by sustained hypoxia, we next examined the underlying pathological changes in the hippocampus. Nissl and haematoxylin–eosin (H&E) staining of fixed brain sections revealed reduced structural integrity of the hippocampus in hypoxia-exposed mice, with loosely arranged neurons, markedly fewer Nissl bodies, and scattered neuronal disorganization and morphological abnormalities—including somatic shrinkage and nuclear hyperchromasia—in the CA1, CA2, CA3, and dentate gyrus (DG) regions. Quantitative analysis confirmed a significant reduction in hippocampal neuron numbers in the hypoxia group (Fig. 2A–B). In contrast, H&E staining of other major organs (heart, liver, spleen, lung, and kidney) revealed no substantial histopathological alterations (Supplementary Fig. S2). To further evaluate neuronal structural integrity, we examined the expression of MAP2, a dendritic cytoskeletal marker, and NeuN, a mature neuronal marker. Immunofluorescence staining revealed a significant reduction in the proportion of cells co-expressing both markers in the hypoxia group compared to the normoxic group (Fig. 2C–D). We next investigated the underlying mechanisms of hypoxia-induced neuronal loss. Given that ferroptosis has been widely implicated in neurological pathologies such as neurodegenerative diseases and traumatic brain injury, we measured the levels of MDA, Fe^{2+}, and total iron in hippocampal tissues of the animal models. Quantitative analysis revealed that, compared with normoxic controls, hippocampal MDA levels, Fe^{2+} content, and total iron content were all significantly elevated in the hypoxia group (Fig. 2E–F), indicating that hypoxic exposure markedly enhances lipid peroxidation and leads to iron accumulation and disruption of iron homeostasis. RT-qPCR and Western blotting were further performed to examine the expression of HIF-1α, a key hypoxia-responsive molecule, and core ferroptosis regulators. The results showed that HIF-1α protein expression was significantly upregulated in the hypoxia group, indicating successful activation of

the hypoxia-responsive pathway. Moreover, the expression of GPX4, a core ferroptosis suppressor, and FTH1, an iron storage protein, was significantly decreased, whereas the expression of ACSL4, a promoter of lipid peroxidation, was significantly increased. Additionally, XCT, a key component of system Xc^-, also tended to decrease, although this change did not reach statistical significance (Fig. 2G–H). Together, these findings indicate that hypoxia-induced hippocampal damage is closely associated with ferroptosis-related molecular alterations, but they do not by themselves establish that ferroptosis occurs; functional validation is therefore required.

3.3 Hypoxia directly damages neuronal mitochondria and promotes mtDNA release into the cytosol

Mitochondrial structural damage and dysfunction are closely associated with the occurrence and development of ferroptosis. To elucidate the key molecular events underlying high-altitude hypoxia-induced cognitive impairment, we established an in vitro hypoxia model using primary hippocampal neurons cultured in a tri-gas incubator (1%O_2). This approach confirmed that hypoxic exposure induces ferroptosis in these neurons (Supplementary Fig. S3). Subsequently, we used the C11-BODIPY 581/591 probe to assess the overall lipid peroxidation level in cells. The red/green fluorescence intensity ratio of neurons in the hypoxia group significantly decreased, indicating a higher state of oxidative stress (Fig. 3A). MAP2 immunofluorescence staining revealed aberrations in the neuronal network structure and synaptic connectivity in the hypoxia group (Fig. 3B). Consistently, transmission electron microscopy revealed intact mitochondrial structures with distinct double membranes and regularly arranged cristae in the normoxia group. In contrast, mitochondria in the hypoxia group were markedly shrunken and exhibited ultrastructural damage, including cristae loss, vacuolar degeneration, and obscured membrane boundaries. Furthermore, quantitative analysis demonstrated significant reductions in mitochondrial area, perimeter, and aspect ratio in the hypoxia group (Fig. 3C). Given that mitochondrial structural damage is often accompanied by bioenergetic metabolic dysfunction, we further conducted Seahorse cell energy metabolism analysis. Compared with the normoxia group, the hypoxia group showed comprehensive declines in basal respiration, ATP production capacity, maximal respiration capacity, and spare respiratory capacity, indicating inhibition of mitochondrial oxidative phosphorylation function. Meanwhile, the coupling efficiency in the hypoxia group decreased, suggesting a reduction in mitochondrial energy conversion efficiency, which may be related to the activation or regulation of proton leakage pathways (Fig. 3D). Additionally, to visualize the release of mitochondrial double-stranded DNA (dsDNA) under hypoxic conditions, we performed immunofluorescence co-staining of dsDNA and the mitochondrial outer membrane marker TOM20. In hippocampal neurons under normoxic conditions, most dsDNA signals co-localized with TOM20-positive mitochondrial regions, indicating that dsDNA was mainly confined within mitochondria under basal conditions. Following hypoxic exposure, the co-localization of dsDNA and TOM20 significantly diminished. Notably, free dsDNA puncta were observed in DAPI-negative cytoplasmic regions, with a significant increase in their abundance relative to the control group (Fig. 3E). These results indicate that hypoxic stress leads to mitochondrial structural damage and promotes mtDNA leakage into the cytoplasm.

3.4 Hypoxia activates the cGAS–STING pathway cell-autonomously in hippocampal neurons

To define how hypoxia precisely triggers neuronal ferroptosis and to map the underlying regulatory network, we performed RNA sequencing (RNA-seq) on primary neurons from the normoxic and hypoxia groups. Biological replicates within each group showed high consistency (Fig. 4A). Relative to normoxic controls, hypoxia upregulated 1,560 and downregulated 1,785 differentially expressed genes (Fig. 4B). KEGG and GO enrichment analyses indicated that hypoxia substantially remodelled the hippocampal transcriptome, with differentially expressed genes enriched in biological processes related to neuronal structural maintenance, intercellular signalling, and synaptic regulation, and in classical pathways associated with energy metabolism, oxidative stress, and cell survival. In addition, several signalling networks related to inflammatory responses and innate immune regulation were significantly enriched, including the cGMP–PKG and chemokine signalling pathways, suggesting that hypoxia may contribute to hippocampal injury by perturbing neuronal homeostasis and intercellular communication (Fig. 4C–E). Taking these transcriptomic findings together with the observed mitochondrial structural damage, impaired oxidative phosphorylation, and aberrant expression of ferroptosis-related molecules, we hypothesised that hypoxia-induced neuronal injury involves the coordinated activation of mitochondrial stress and inflammatory–immune signalling. In the mouse hypoxia model, Western blotting showed decreased mitochondrial TOM20, significantly increased cGAS expression, and pronounced increases in phosphorylated STING, TBK1, and IRF3 (Fig. 4F); RT-qPCR yielded concordant results at the transcriptional level (Fig. 4G). Mitochondrial damage-induced mtDNA release is an established mechanism for activating the cGAS–STING innate immune pathway. Next, significantly enhanced cytosolic dsDNA signal was observed in the DG, CA1, CA2, and CA3 regions of the hippocampus (Fig. 4H). Because cytosolic DNA is the canonical ligand of cGAS, we next examined STING pathway activation. Immunofluorescence showed markedly enhanced p-STING signal across hippocampal subregions in the hypoxia group (Fig. 4I). Notably, whereas cGAS–STING is conventionally regarded as a key inflammatory pathway in immune cells, our data support its cell-autonomous activation in neurons: p-STING immunofluorescence was highly co-localised with the neuronal marker NeuN; Moreover, hypoxia alone was sufficient to induce STING–TBK1–IRF3 phosphorylation in primary neurons (Supplementary Fig. S4).

To further explore transcriptomic remodelling across the complete hippocampal cell lineage under hypoxia, we performed an exploratory re-analysis of a publicly available single-cell RNA-seq dataset of neonatal hypoxic mouse hippocampus. UMAP (Uniform Manifold Approximation and Projection) dimensionality reduction identified multiple hippocampal cell populations, including neurons, astrocytes, oligodendrocytes, oligodendrocyte precursor cells, and microglia (Fig. 4J). Module scoring showed that gene sets related to STING activation, mitochondrial damage, and ferroptosis were markedly enriched in the neuronal population after hypoxia, with an even greater effect in the ischaemia–hypoxia group (Fig. 4K). These observations are consistent with our finding of STING activation, mitochondrial damage, and ferroptosis, and support a model in which hypoxia induces mitochondrial damage, leading to mtDNA

release into the cytosol and subsequent activation of cGAS–STING signalling. Because this analysis is exploratory and derived from an independent dataset with distinct experimental conditions, it should be interpreted as supportive rather than definitive evidence.

3.5 Mitochondrial damage precedes cGAS–STING activation and ferroptosis in the hypoxic hippocampus

To determine whether cGAS–STING activation is merely a concomitant phenomenon of hypoxia-induced neuronal injury or a critical regulatory node in disease progression, we treated hypoxia-exposed mice with the STING-specific inhibitor C-176 (a covalent inhibitor that targets cysteine of mouse STING) (Fig. 5A). Behavioural testing and histological analysis after modelling showed that, compared with the hypoxia group, C-176-treated mice exhibited partial recovery of brain weight and attenuated body weight loss (Fig. 5B–C), indicating that STING inhibition improves the overall physiological state under hypoxia. Behaviourally, C-176 treatment reversed the hypoxia-induced impairments in nesting structure integrity, T-maze correct-choice rate, NOR exploration preference, and MWM spatial memory (Fig. 5D–G), indicating that STING inhibition ameliorates hypoxia-induced cognitive deficits. TEM revealed marked mitochondrial shrinkage and reduced cristae in the hypoxia group, whereas C-176 treatment substantially improved mitochondrial structural integrity, with significant recovery of mitochondrial area, perimeter, and aspect ratio (Fig. 5H). At the molecular level, hypoxia significantly increased the p-STING/STING, p-TBK1/TBK1, and p-IRF3/IRF3 ratios, all of which were significantly reduced by C-176, confirming effective suppression of the downstream inflammatory signalling cascade. Importantly, in both the mouse model and primary neurons, STING inhibition partially ameliorated canonical ferroptosis features (Fig. 5I-J and Supplementary Fig. S5). Moreover, in our time-course hypoxia model, hippocampal mitochondrial damage preceded both cGAS–STING activation and ferroptosis (Supplementary Fig. S5), indicating that mitochondrial injury is the earliest event in this sequence. Together, these results indicate that STING inhibition not only alleviates hypoxia-induced cognitive deficits but also improves mitochondrial structural damage, identifying cGAS–STING signalling as an upstream event of ferroptosis in hypoxia-induced neuronal injury.

3.6 Ferroptosis inhibition attenuates hypoxia-induced cognitive impairment and neuronal loss

To further determine whether ferroptosis is a key molecular process in high-altitude hypoxia-associated cognitive impairment, we treated hypoxia-exposed mice with the ferroptosis inhibitor liproxstatin-1 (LIP-1) (Fig. 6A). After modelling, behavioural and histological analyses showed that brain and body weights were partially restored in LIP-1-treated mice relative to the hypoxia group (Fig. 6B–C). The hypoxia-induced decline in nesting ability was markedly improved by LIP-1, with restored nest structural integrity and significantly higher nesting scores (Fig. 6D). LIP-1 treatment also significantly increased T-maze correct-choice rate (Fig. 6E) and improved the NOR time, distance, and exploration-frequency indices (Fig. 6F), and partially restored MWM spatial exploration and spatial memory deficits (Fig. 6G). Western blotting of hippocampal tissue showed that, compared with the hypoxia group, LIP-1 treatment tended to

reduce HIF-1α protein levels, although this did not reach statistical significance, and partially reversed the expression of the ferroptosis markers GPX4 and FTH1 (Fig. 6H). To further verify the protective effect of ferroptosis inhibition on neuronal damage, we examined the neuronal marker NeuN. Immunofluorescence showed that NeuN-positive neurons were markedly reduced in the CA1, CA2, CA3, and DG regions of the hypoxia group, whereas LIP-1 treatment significantly increased the number of NeuN-positive cells across hippocampal subregions (Fig. 6I). LIP-1 also attenuated hypoxia-induced mitochondrial ultrastructural damage, such as swelling and cristae disruption (Fig. 6J), and partially reversed lipid peroxidation levels and mitochondrial energy metabolism (Supplementary Fig. S6).

These results indicate that inhibiting ferroptosis plays a critical role in ameliorating hypoxia-induced hippocampal neuronal loss and cognitive impairment. Given that LIP-1 is a radical-trapping antioxidant whose protective effects are not strictly ferroptosis-specific, and that we did not observe any change in p-STING/p-TBK1 activation following LIP-1 treatment (Supplementary Fig. S6), we propose that mitochondrial damage and ferroptosis are functionally coupled, with STING activation acting upstream; the precise nature of this coupling warrants further investigation.

3.7 STING interacts with CISD1 to regulate neuronal iron homeostasis and ferroptosis

The aforementioned results have robustly demonstrated that activation of the cGAS-STING signaling pathway and neuronal ferroptosis play pivotal roles in hypoxic cognitive dysfunction. However, the nature of the regulatory relationship between these two mechanisms—whether direct or indirect—remains elusive. The research team used STING-specific antibodies to conduct a combined Co-IP and proteomics analysis on hippocampal tissues from the hypoxia-exposed group and hypoxic primary neurons. These results were cross-referenced with a ferroptosis database; subsequent Venn diagram analysis identified nine potential key molecules (Fig. 7A). Subsequently, a protein-protein interaction (PPI) network map was constructed, and the analysis results showed that CISD1 forms a tight interaction network with iron metabolism and mitochondrial homeostasis regulatory molecules (Fig. 7B). To assess the potential association of these candidates with STING, we performed molecular docking of the nine candidate protein structures with STING. CISD1 showed the highest binding score and the most stable predicted conformation among all candidates (Fig. 7C), and three-dimensional structural analysis indicated multiple stable hydrogen bonds and hydrophobic interaction sites between CISD1 and STING (Fig. 7D). These computational predictions suggest a possible direct interaction, which we subsequently validated experimentally. We therefore focused on CISD1 and examined its expression in the animal model. Immunofluorescence showed only low-level CISD1 expression in the CA1, CA2, CA3, and DG regions of the hippocampus under normoxia, whereas CISD1 signal was markedly enhanced across all hippocampal subregions after hypoxia (Fig. 7E). Western blotting confirmed a significant increase in hippocampal CISD1 protein in the hypoxia group (Fig. 7F), consistent with the observed mitochondrial damage and ferroptosis. To determine whether STING and CISD1 physically interact, we performed co-immunoprecipitation, which showed basal STING–CISD1 binding under normoxia that was significantly enhanced after hypoxia (Fig. 7G), and immunofluorescence co staining suggested that the two proteins

were co localized in the hypoxic group (Fig. 7H). The above results suggest that hypoxic stress promotes the formation of a stable complex between the two proteins. On this basis, we propose that STING may bind CISD1 and impair its iron-homeostatic function, thereby promoting neuronal ferroptosis under hypoxia. Given that STING resides at the ER and is enriched at mitochondria-associated membranes, which lie in close proximity to the outer mitochondrial membrane where CISD1 localises, such an interaction is spatially plausible.

3.8 Systemic metabolic and inflammatory alterations in high-altitude populations

To assess the potential clinical relevance of STING-related signalling in hypoxia-induced neuronal injury, we performed a clinical cohort study. Serum biochemical profiling of individuals from different altitude cohorts showed varying degrees of abnormality in hepatic function, lipid metabolism, and inflammation-related indices in the high-altitude group (Fig. 8A), characterised by significantly reduced total protein, albumin, and cholesterol levels and a trend toward elevated inflammatory indices, suggesting that chronic hypoxia induces systemic metabolic disturbance and inflammation that may provide a pathological substrate for hypoxic neuronal injury. Serum proteomic analysis of low- (L), middle- (M), and high-altitude (H) groups showed clear separation of samples by principal component analysis (Fig. 8B). Among them, a total of 2,229 differentially expressed proteins were identified between the high- and low-altitude groups, of which 911 were upregulated and 1,318 downregulated (Fig. 8C). Functional annotation revealed enrichment in biological processes related to mitochondrial stress, hypoxia-associated metabolic reprogramming, endoplasmic reticulum translocation, and ferroptosis (Fig. 8D). Notably, several gene modules associated with mitochondrial homeostasis, ROS generation, and innate immune activation were markedly altered, suggesting that mitochondrial damage and inflammatory signalling may jointly contribute to hypoxia-associated neuronal injury. Serum MDA and iron levels also increased with altitude (Fig. 8E). These findings suggest that targeting ferroptosis and immune–inflammatory signalling may offer new therapeutic opportunities for the prevention and treatment of high-altitude hypoxic cognitive impairment.

4. Discussion

Cognitive dysfunction is one of the major neurological pathological manifestations induced by high-altitude hypoxia exposure. The hippocampus, in particular, has been established as a brain region highly sensitive to hypoxia and oxidative stress injury, playing a central role in spatial learning, memory consolidation, and episodic memory[25–27]. In the present study, we established a complete pathological axis from organelle damage to regulated cell death in the context of high-altitude hypoxia, systematically revealing the intrinsic links among hypoxia-induced hippocampal neuronal injury, mitochondrial dysfunction, cGAS–STING pathway activation, and ferroptosis (Fig. 9).

First, through a series of behavioral experiments, we found that learning and memory abilities were significantly impaired in mice after hypoxia exposure, indicating that this animal model successfully

recapitulated the phenotype of hypoxic cognitive impairment (Fig. 1). Furthermore, consistent findings from HE staining, Nissl staining, and immunofluorescence staining for MAP2 and NeuN indicated that hypoxia not only reduced neuronal numbers but also potentially compromised the structural basis of synaptic connections and network architecture (Fig. 2). These results are consistent with previous reports that hypoxia induces cerebral energy metabolism dysfunction, oxidative stress, and neurological decline[28]. Meanwhile, ferroptosis was identified as an important mode of cell death underlying hypoxia-induced hippocampal neuronal injury in this study. Following hypoxia exposure, MDA and iron levels were elevated in the mouse hippocampus, accompanied by aberrant expression of ferroptosis-related marker molecules (Fig. 2). More importantly, intervention with a ferroptosis inhibitor significantly ameliorated hypoxia-induced cognitive behavioral abnormalities and reduced the loss of NeuN-positive neurons (Fig. 6). This finding not only demonstrates an association between ferroptosis and hypoxic neuronal injury but also indicates a functional contribution of ferroptosis to hypoxic cognitive impairment. Given that neurons are rich in polyunsaturated fatty acids and have relatively limited antioxidant capacity, they may be more susceptible to undergoing ferroptosis once the balance between iron homeostasis and lipid peroxidation is disrupted[29,30]. Therefore, ferroptosis may represent an important pathological basis for hippocampal neuronal injury under high-altitude hypoxic conditions.

Under hypoxic conditions, insufficient oxygen supply as the terminal electron acceptor of mitochondrial oxidative phosphorylation constrains electron transport chain efficiency, leading to reduced oxidative phosphorylation-mediated ATP production; concurrently, electron leakage from the electron transport chain drives increased mitochondrial reactive oxygen species generation[31]. As an important organelle for sensing and amplifying hypoxic stress signals, mitochondria generate reactive oxygen species that participate in the regulation of the HIF-1 pathway[32]; under sustained severe hypoxia exposure, mitochondrial structure and function are prone to damage[33]. In the present study, transmission electron microscopy revealed ultrastructural damage to neuronal mitochondria after hypoxia exposure, and Seahorse energy metabolism analysis confirmed abnormal mitochondrial respiratory function in hypoxic primary neurons (Fig. 3), collectively providing permissive conditions for ferroptosis. Meanwhile, impaired mitochondrial membrane integrity led to the release of intramitochondrial dsDNA into the cytosol, which, upon recognition by the cytosolic DNA sensor cGAS, subsequently activated the cGAS–STING signaling pathway (Fig. 4). Consistent with this, *in vivo* experiments demonstrated that STING inhibitor administration significantly improved cognitive function and attenuated hippocampal neuronal ferroptosis in hypoxic mice (Fig. 5), indicating that the cGAS–STING pathway acts not merely as a responder to hypoxic stress but also positions STING as an upstream regulator of ferroptosis. Furthermore, previous studies have largely regarded cGAS–STING as an effector arm of immune cells and inflammatory responses[34,35], yet its cellular attribution in the brain has long been controversial. The present study supports neuron-autonomous activation. Specifically, p-STING immunofluorescence signals showed high co-localization with NeuN; in primary neurons, hypoxia alone was sufficient to induce STING–TBK1–IRF3 phosphorylation, and inhibition of STING was sufficient to alleviate ferroptosis. Furthermore, public single-cell data revealed significantly elevated STING pathway module scores in neuronal subpopulations. Notably, we do not contend that microglia are entirely uninvolved—

hypoxia can also induce microglial activation, and microglia-derived type I interferons may further sensitize neuronal ferroptosis through paracrine mechanisms. The relative contributions of neurons and microglia to this pathway require detailed dissection using cell type-specific conditional knockout models (e.g., Sting1$^{fl/fl}$;Camk2-Cre and Cx3cr1-CreER), which represents a limitation of our study. Collectively, our study extends the effector spectrum of cGAS–STING from interferon-dependent inflammatory responses to ferroptosis, echoing recently reported associations between STING and lipid peroxidation in cancer and liver injury, and establishes the causal contribution of this hierarchical relationship to cognitive phenotypes. Subsequently, CISD1 was identified as a key bridging molecule through co-immunoprecipitation and proteomic analyses in this study. Its iron–sulfur cluster structure can be transferred to acceptor proteins under oxidative or acidifying conditions, thereby participating in the regulation of mitochondrial iron metabolism, redox homeostasis, and energy metabolism[36]. Hypoxic conditions significantly enhanced the binding between STING and CISD1; structural biology predictions also suggested physical interaction between the two proteins (Fig. 7). These findings suggest that under hypoxic conditions, CISD1 may participate in the formation of STING-associated protein complexes and serve as a bridge between cGAS–STING signaling and ferroptosis. It should be noted that CISD1 may play complex roles in different disease and cellular contexts[18,19,37]: its upregulation may represent a compensatory cellular response to mitochondrial iron homeostasis dysregulation, or it may participate in pathological signal amplification through aberrant protein interactions. Therefore, the precise function of CISD1 in hypoxic neuronal ferroptosis requires further clarification through experiments involving CISD1 overexpression, knockdown, or site-directed mutagenesis of specific residues. Finally, in a human cohort, we found that serum markers of iron and oxidative damage increased with rising residential altitude (Fig. 8), suggesting that the findings from animal and cellular experiments have certain translational relevance to human populations. This finding provides a potential direction for the screening of early biomarkers of high-altitude hypoxia-related cognitive impairment. However, serum proteins are primarily derived from the liver and blood cells, and their changes do not necessarily reflect pathological alterations in hippocampal neurons. Future studies should expand the sample size and conduct multivariate analyses incorporating cognitive scales, blood oxygen saturation, exposure duration, and neuroimaging to establish the reliability of these molecules as predictive or diagnostic indicators.

Collectively, the evidence suggests that hypoxic neuronal injury is not a linear cascade but rather a self-amplifying loop: mitochondrial damage releases mtDNA to activate STING, which, through interaction with CISD1, exacerbates mitochondrial iron overload and lipid peroxidation; the resulting ferroptotic stress further disrupts mitochondrial integrity and releases more mtDNA. Nevertheless, several limitations of this study should be acknowledged: (1) The current findings are primarily based on pharmacological inhibitor interventions. Although both ferroptosis and STING inhibitors demonstrated protective effects, potential off-target effects of these drugs cannot be excluded, and future studies should incorporate genetic knockout or virus-mediated cell-specific interventions for validation; (2) The interaction between CISD1 and STING is currently supported mainly by co-immunoprecipitation, proteomic profiling, and molecular docking analyses, and requires further confirmation through proximity ligation assays or co-localization super-resolution imaging. Furthermore, the functional roles of the other

8 candidate molecules identified by Co-IP screening and their potential synergistic mechanisms in the cGAS–STING pathway remain unexplored; (3) This study focused on hippocampal neurons, but hypoxic cognitive impairment also involves microglia, astrocytes, cerebrovascular endothelial cells, and blood–brain barrier dysfunction. Future studies employing single-cell sequencing or spatial transcriptomics could elucidate intercellular interaction mechanisms; (4) The human data presented in this study are derived from a cross-sectional cohort of young individuals and lack corroboration from neuroimaging. Despite these limitations, the present study reveals that hypoxia mediates cognitive dysfunction through a self-amplifying pathological axis of "mitochondrial damage–mtDNA release–cGAS/STING activation–CISD1 interaction–neuronal ferroptosis," and suggests that this regulatory axis represents a potential therapeutic target. Given that the current evidence is derived from rodent models and cross-sectional human data, the clinical value of this axis awaits prospective studies and translational validation.

Abbreviations

CISD1 CDGSH iron
sulfur domain-containing protein 1

Declarations

Ethics approval and consent to participate

The study was approved by the guidelines of the Biomedical Ethics Committee of Xizang Minzu University (approval no. 2026-03-003).

Competing Interests

The authors declare that they have no competing financial interests or personal relationships that could have appeared to influence the work reported in this paper.

Funding statement

Supported by the Science and Technology Projects of Xizang Autonomous Region (XZ202502JD0034); National Natural Science Foundation of China (32660248); Xizang Natural Science Foundation (XZ202501ZR0089); Project of Xizang Minzu University (25MDX02; 25XZMDQD10; Y2026172).

Author Contribution

QC and JMS designed the experiments and wrote the manuscript. HDZ, YXL, JQL and SCQ performed the animal experiments. YJF and YYZ carried out the cellular experiments. HDZ, HL and ZJ performed the molecular experiments. XKH provided all serological clinical test results. HDZ analyzed all

experimental data. HM, CRY and YZ provided methodological technical support and conducted a critical review of the manuscript. All authors have read and approved the final manuscript.

Data Availability

The dataset used and analyzed in this study can be provided by the corresponding author upon reasonable request.

References

1. Gatterer H, et al. Altitude illnesses. Nat reviews Disease primers. 2024;10:43.
2. Cai C, et al. Altitude hypoxia and hypoxemia: pathogenesis and management. Signal Transduct Target therapy. 2026;11:27.
3. Zhang X, et al. Brain Structural and Functional Alterations in Native Tibetans Living at High Altitude. Neuroscience. 2023;520:134–43.
4. Wszedybyl-Winklewska M et al. Mild chronic hypoxia and the brain: an ambiguous relationship. J Neuroinflamm (2026).
5. Zhang J et al. High-Altitude Hypoxia Injury: Systemic Mechanisms and Intervention Strategies on Immune and Inflammatory Responses. Antioxidants 15(2025).
6. Mima D, et al. Prevalence and risk factors for dementia in the Tibetan region: A population-based cross-sectional study. J Affect Disord. 2023;334:159–65.
7. Dixon SJ, et al. Ferroptosis: an iron-dependent form of nonapoptotic cell death. Cell. 2012;149:1060–72.
8. Zhang Z, et al. CGI1746 targets sigma(1)R to modulate ferroptosis through mitochondria-associated membranes. Nat Chem Biol. 2024;20:699–709.
9. Ward RJ, Zucca FA, Duyn JH, Crichton RR, Zecca L. The role of iron in brain ageing and neurodegenerative disorders. Lancet Neurol. 2014;13:1045–60.
10. Weiland A, et al. Ferroptosis and Its Role in Diverse Brain Diseases. Mol Neurobiol. 2019;56:4880–93.
11. Lei P, Walker T, Ayton S. Neuroferroptosis in health and diseases. Nat Rev Neurosci. 2025;26:497–511.
12. Khan S, et al. Oxytosis/Ferroptosis, and Neurodegeneration: Emerging Insights into Mitochondrial Mechanisms. Aging disease. 2024;16:2504–43. Excitotoxicity.
13. Hu MM, Shu HB. Mitochondrial DNA-triggered innate immune response: mechanisms and diseases. Cell Mol Immunol. 2023;20:1403–12.
14. Li H, Cai R, Zhou Y, Jiang Y, Tan S. cGAS-STING signaling in brain aging and neurodegeneration: molecular links and therapeutic perspectives. J Neuroinflamm. 2025;22:235.

15. Gulen MF, et al. cGAS-STING drives ageing-related inflammation and neurodegeneration. Nature. 2023;620:374–80.
16. West AP, et al. Mitochondrial DNA stress primes the antiviral innate immune response. Nature. 2015;520:553–7.
17. Catapano A, et al. Iron metabolism and ferroptosis in health and diseases: The crucial role of mitochondria in metabolically active tissues. J Nutr Biochem. 2025;140:109888.
18. Bitar S et al. Iron-sulfur cluster loss in mitochondrial CISD1 mediates PINK1 loss-of-function phenotypes. eLife 13(2024).
19. Zhang X, et al. Inhibition of CISD1 alleviates mitochondrial dysfunction and ferroptosis in mice with acute lung injury. Int Immunopharmacol. 2024;130:111685.
20. Zang J, Cui M, Xiao L, Zhang J, Jing R. Overexpression of ferroptosis-related genes FSP1 and CISD1 is related to prognosis and tumor immune infiltration in gastric cancer. Clin translational oncology: official publication Federation Span Oncol Soc Natl Cancer Inst Mexico. 2023;25:2532–44.
21. Martinez A, et al. Mitochondrial CISD1/Cisd accumulation blocks mitophagy and genetic or pharmacological inhibition rescues neurodegenerative phenotypes in Pink1/parkin models. Mol neurodegeneration. 2024;19:12.
22. Ishikawa H, Barber GN. STING is an endoplasmic reticulum adaptor that facilitates innate immune signalling. Nature. 2008;455:674–8.
23. Liu JY, et al. Organelle-orchestrated cGAS-STING signaling and its role in neurodegeneration. Pharmacol Res. 2026;228:108216.
24. Tamir S, et al. Structure-function analysis of NEET proteins uncovers their role as key regulators of iron and ROS homeostasis in health and disease. Biochim Biophys Acta. 2015;1853:1294–315.
25. Magee JC. Behavioral timescale synaptic plasticity: properties, elements and functions. Nat Neurosci (2026).
26. Irving A, Harvey J. Regulation of hippocampal synaptic function by the metabolic hormone leptin: Implications for health and disease. Prog Lipid Res. 2021;82:101098.
27. Burtscher J, Mallet RT, Burtscher M, Millet GP. Hypoxia and brain aging: Neurodegeneration or neuroprotection? Ageing Res Rev. 2021;68:101343.
28. Semenza GL. Hypoxia-inducible factors in physiology and medicine. Cell. 2012;148:399–408.
29. Stockwell BR, et al. Ferroptosis: A Regulated Cell Death Nexus Linking Metabolism, Redox Biology, and Disease. Cell. 2017;171:273–85.
30. Zhang M, et al. Synchronously Evoking Disulfidptosis and Ferroptosis via Systematical Glucose Deprivation Targeting SLC7A11/GSH/GPX4 Antioxidant Axis. ACS Nano. 2025;19:14233–48.
31. Schieber M, Chandel NS. ROS function in redox signaling and oxidative stress. Curr biology: CB. 2014;24:R453–462.
32. Huang X, Zhao L, Peng R. Hypoxia-Inducible Factor 1 and Mitochondria: An Intimate Connection. Biomolecules 13(2022).

33. Wszedybyl-Winklewska M et al. Mild chronic hypoxia and the brain: an ambiguous relationship. J Neuroinflamm 23(2026).
34. Yang NS, et al. mtDNA-cGAS-STING axis-dependent NLRP3 inflammasome activation contributes to postoperative cognitive dysfunction induced by sevoflurane in mice. Int J Biol Sci. 2024;20:1927–46.
35. Negishi H, et al. cGAS-IFN-I responses by extracting nuclear DNA from dying cells via nucleocytosis. Nat Commun. 2026;17:1658.
36. Paddock ML, et al. MitoNEET is a uniquely folded 2Fe 2S outer mitochondrial membrane protein stabilized by pioglitazone. Proc Natl Acad Sci USA. 2007;104:14342–7.
37. Zhang ZB, et al. MiR-127-3p targeting CISD1 regulates autophagy in hypoxic-ischemic cortex. Cell Death Dis. 2021;12:279.

Figures

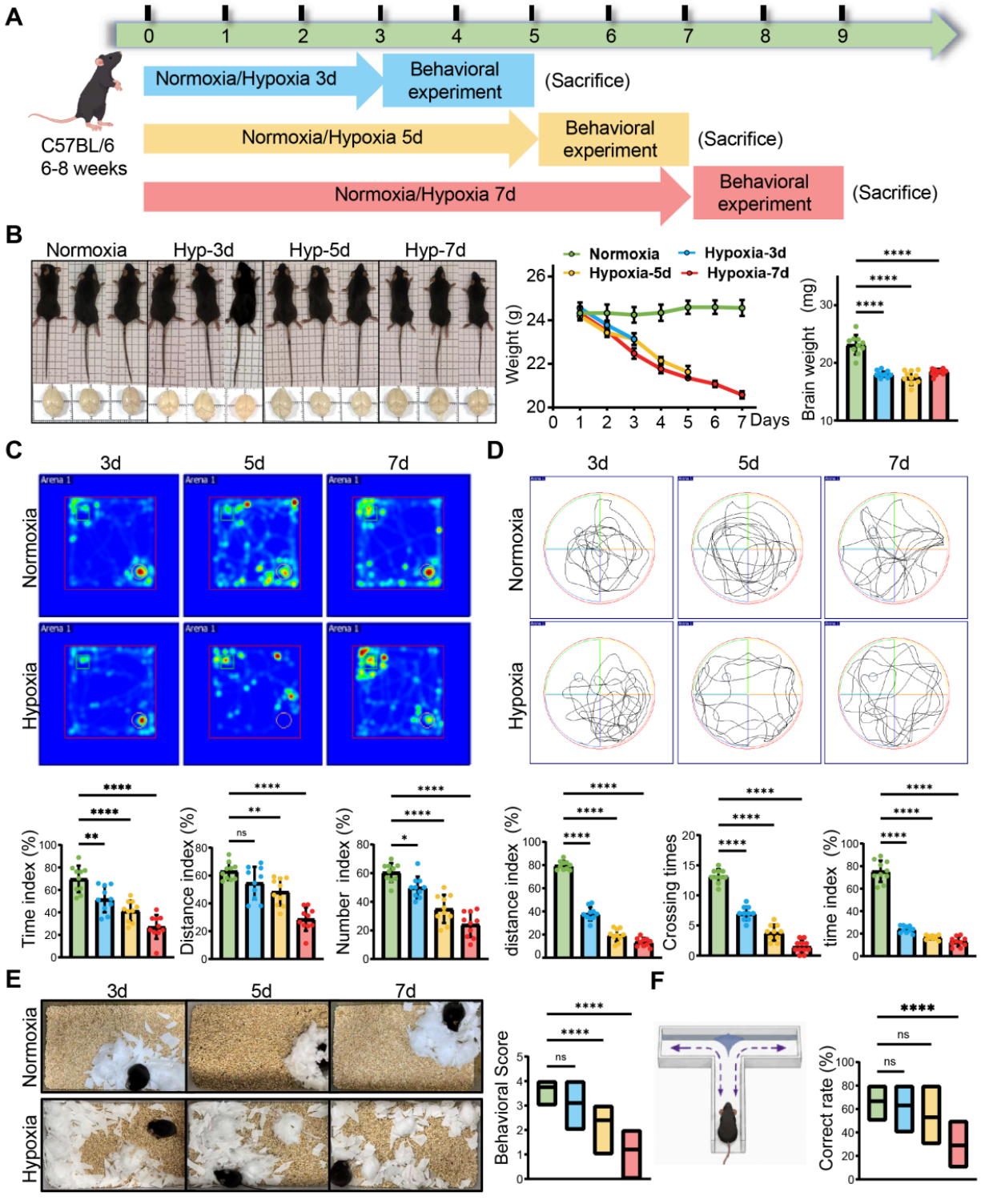


Figure 1

Hypoxic exposure induces cognitive impairment in mice.

A, Experimental scheme of the hypoxic animal model. Male C57BL/6 mice (6–8 weeks old) were exposed to normoxia or a simulated 6000-m high-altitude hypoxic environment for 3, 5, or 7 d, and behavioral tests and tissue collection were performed at the corresponding time points (n = 10 mice per

group). B, Representative images of mice and brain tissues, dynamic changes in body weight during hypoxic exposure, and quantification of brain weight after modeling. C, Representative activity heatmaps of the novel object recognition (NOR) test and quantification of the time index, distance index, and exploration count index. D, Representative swimming trajectories in the Morris water maze (MWM) spatial probe test and quantification of the target-quadrant distance index, the number of crossings over the former platform location, and the target-quadrant time index. E, Representative images of the nest building test and nesting behavior scores. F, Schematic diagram of the T-maze test and quantification of the correct choice rate. Body weight data were analyzed by two-way repeated-measures ANOVA; other comparisons were analyzed by one-way ANOVA followed by appropriate post hoc multiple comparisons. Brown–Forsythe and Bartlett tests were used to assess homogeneity of variances. ns, not significant; *P < 0.05, **P < 0.01, ****P < 0.0001.

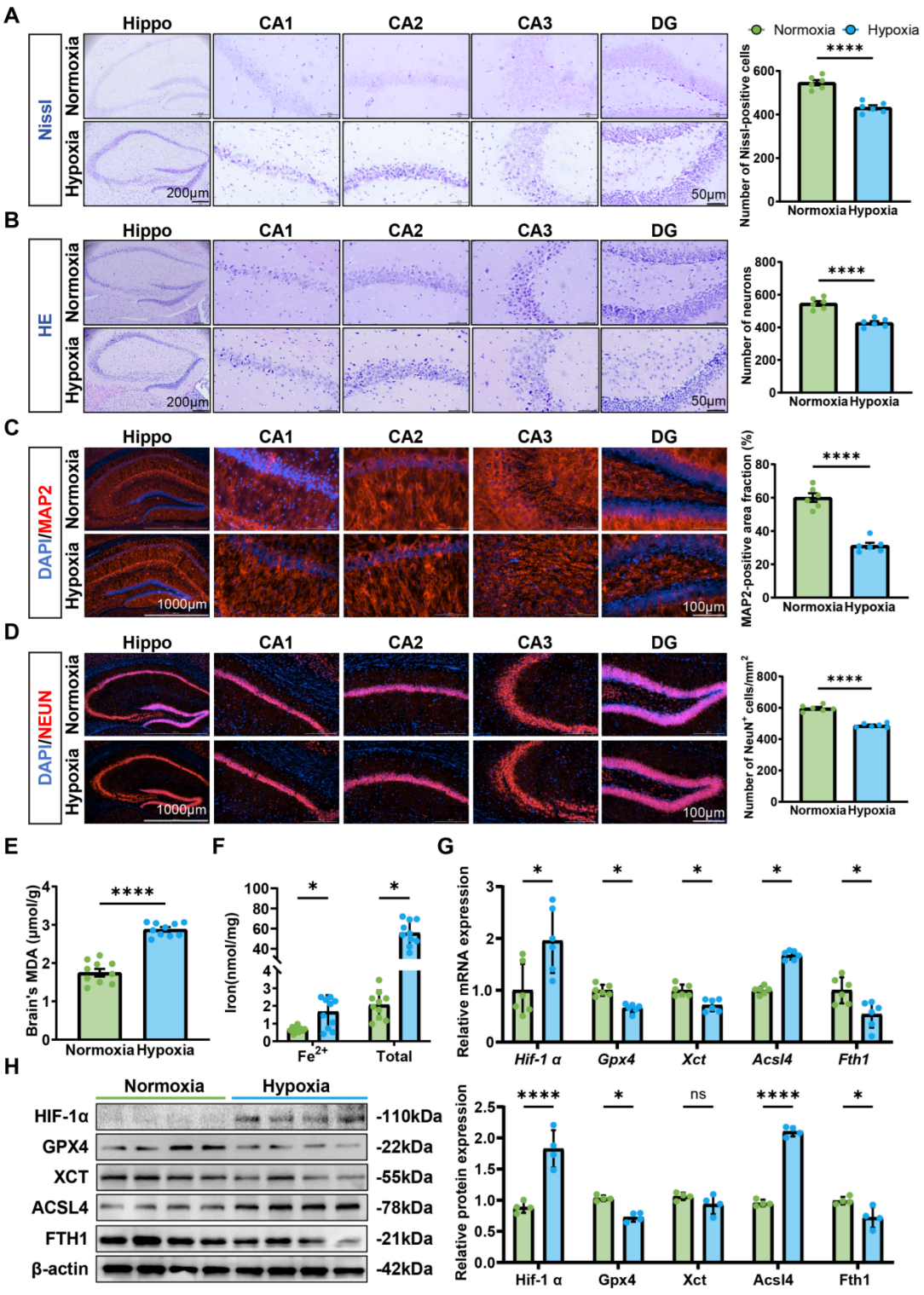


Figure 2

Hypoxia induces hippocampal neuronal injury and ferroptosis-related alterations.

A, Representative Nissl staining images of the hippocampus and its subregions (CA1, CA2, CA3, and dentate gyrus (DG)) in normoxic and hypoxic mice and quantification of Nissl-positive neurons. Scale bars: 200 μm (hippocampus) and 50 μm (subregions). B, Representative H&E staining images of the

hippocampus and quantification of morphologically intact neurons. Scale bars: 200 μm and 50 μm. C, Representative immunofluorescence images of MAP2 (red) and DAPI (blue) in hippocampal subregions and quantification of MAP2-positive signals. D, Representative immunofluorescence images of NeuN (red) and DAPI (blue) and quantification of NeuN-positive neurons. E–F, Hippocampal malondialdehyde (MDA) levels, Fe^{2+}, and total iron contents in normoxic controls and hypoxic mice (n = 10). G, Relative mRNA expression levels of *Hif1a*, *Gpx4*, *Xct/Slc7a11*, *Acsl4*, and *Fth1* detected by RT–qPCR (n = 6). H, Representative Western blots of the corresponding proteins in hippocampal tissues and densitometric quantification, with β-actin as loading control (n = 4). ns, not significant; *P < 0.05, ****P < 0.0001.

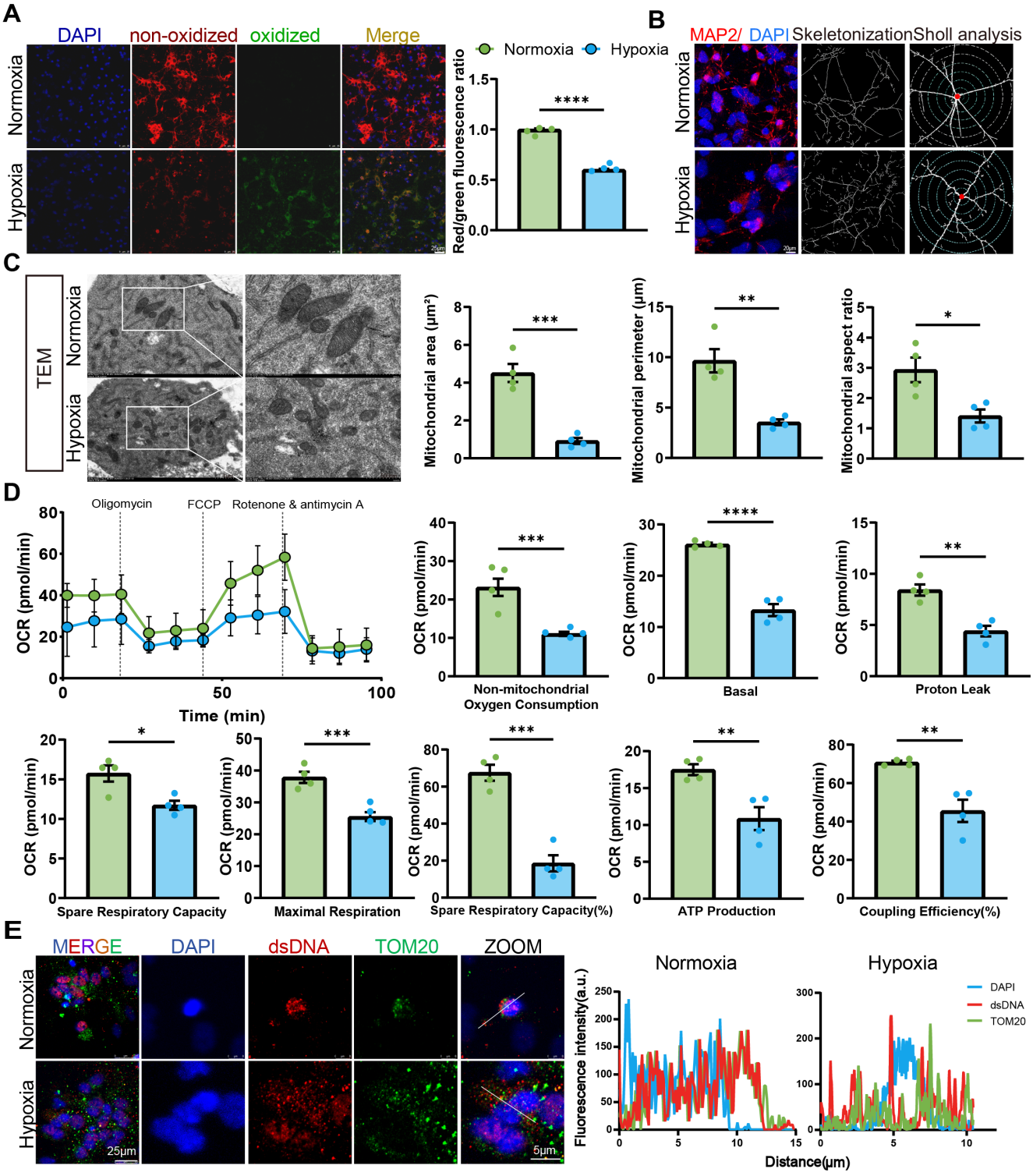


Figure 3

Hypoxia impairs mitochondrial structure and bioenergetic function and promotes mitochondrial DNA release in primary hippocampal neurons.

A, Representative C11-BODIPY 581/591 fluorescence images of primary hippocampal neurons cultured under normoxic or hypoxic conditions for 24 h (unoxidized signal, red; oxidized signal, green) and

quantification of the red/green fluorescence intensity ratio. B, Representative MAP2 immunofluorescence images and neurite skeletonization analysis in the normoxic and hypoxic groups. C, Representative transmission electron microscopy (TEM) images of neuronal mitochondria and quantification of mitochondrial area, perimeter, and aspect ratio. D, Oxygen consumption rate (OCR) curves from the Seahorse mitochondrial stress test, with sequential injections of oligomycin, FCCP, and rotenone/antimycin A, and quantification of non-mitochondrial oxygen consumption, basal respiration, proton leak, spare respiratory capacity, maximal respiration, ATP production, and coupling efficiency. E, Representative immunofluorescence images of dsDNA (red), TOM20 (green), and DAPI (blue) and line-scan fluorescence intensity profiles, showing the subcellular redistribution of mitochondrial DNA after hypoxia. Comparisons between the two groups were performed using unpaired t-tests; n = 4 independent biological replicates for all experiments. *P < 0.05, **P < 0.01, ***P < 0.001, ****P < 0.0001.

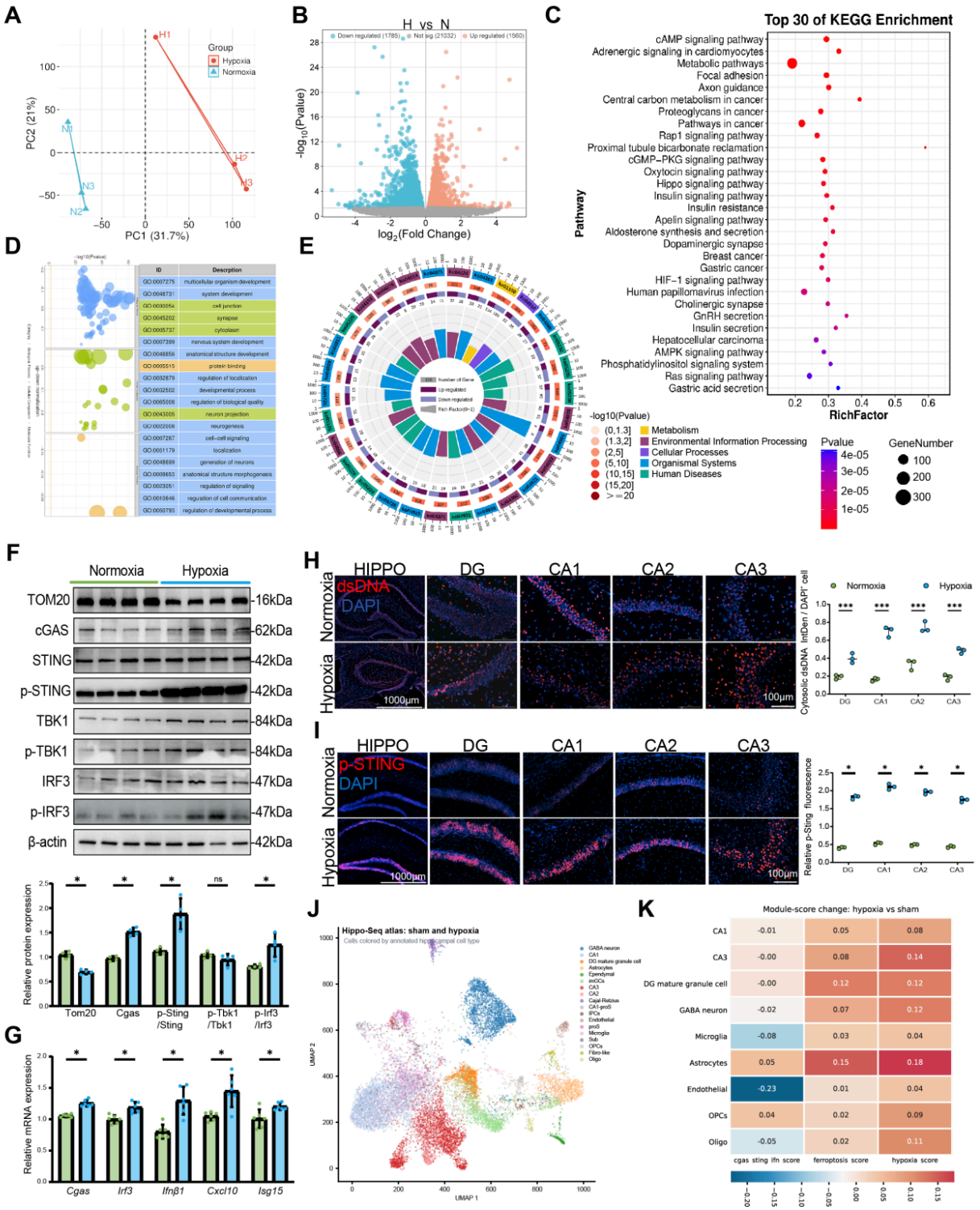


Figure 4

Hypoxic stress activates the cGAS–STING signaling pathway in neurons.

A, Principal component analysis (PCA) of RNA-seq data from primary hippocampal neurons in the normoxic and hypoxic groups (n = 3). B, Volcano plot of differentially expressed genes between the hypoxic and normoxic groups. C, KEGG pathway enrichment analysis of differentially expressed genes.

D–E, Functional annotation and enrichment analysis of hypoxia-responsive transcripts. F, Representative Western blots and quantification of TOM20, cGAS, p-STING/STING, p-TBK1/TBK1, and p-IRF3/IRF3 in hippocampal tissues. Phosphorylated proteins were normalized to the corresponding total proteins, and non-phosphorylated proteins were normalized to β-actin (n = 4). G, RT–qPCR analysis of cGAS–STING-related gene expression in hippocampal tissues (n = 6). H, Representative immunofluorescence images and quantification of cytosolic dsDNA in the hippocampus and its subregions DG, CA1, CA2, and CA3 (n = 3). I, Representative immunofluorescence images and quantification of p-STING in the hippocampus and its subregions (n = 3). J, UMAP visualization of cell clusters from re-analysis of an independent public single-cell RNA sequencing dataset of the hippocampus from neonatal hypoxic mice. K, Module scores of mitochondrial damage-, STING signaling-, and ferroptosis-related gene sets in different cell clusters. Comparisons between the two groups were performed using unpaired t-tests. *P < 0.05, **P < 0.01, ***P < 0.001, ****P < 0.0001.

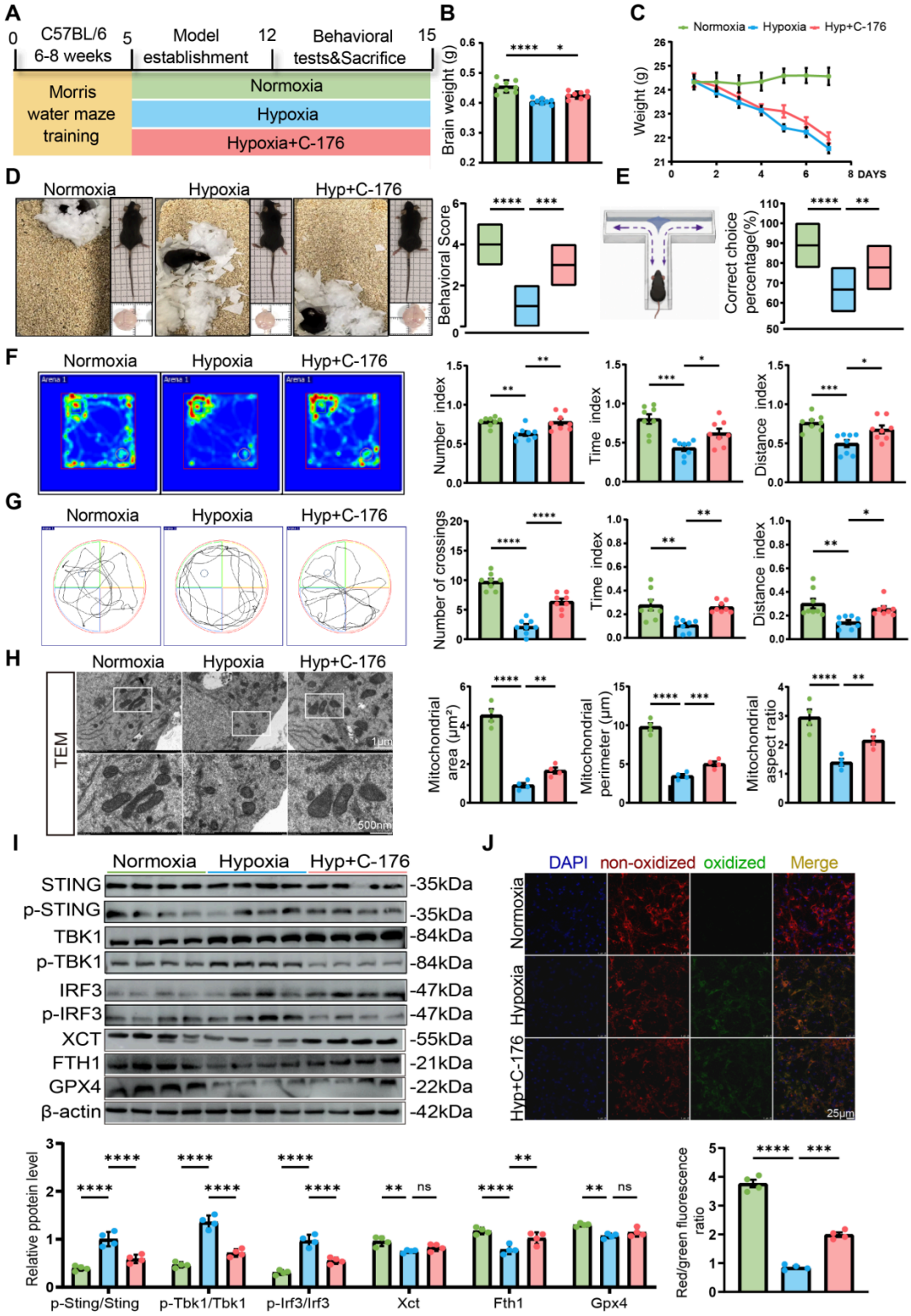


Figure 5

Inhibition of STING alleviates hypoxia-induced cognitive impairment, mitochondrial damage, and ferroptosis-related phenotypes.

A, Experimental scheme of C-176 intervention in hypoxic mice; C-176 was administered by intraperitoneal injection at 10 mg/kg once daily for 7 consecutive days. B, Brain weights of mice in the

normoxia, hypoxia, and hypoxia + C-176 groups. C, Dynamic changes in body weight in each group. D, Representative images of the nest building test and behavioral scores. E, Schematic diagram of the T-maze test and correct choice rate. F, Representative activity heatmaps of the NOR test and quantification of the exploration count, time, and distance indices. G, Representative swimming trajectories in the MWM spatial probe test and quantification of platform-site crossings, time index, and distance index. H, Representative TEM images of primary hippocampal neurons treated with normoxia, hypoxia, or hypoxia + C-176 and quantification of mitochondrial area, perimeter, and aspect ratio. I, Representative Western blots and quantification of p-STING/STING, p-TBK1/TBK1, p-IRF3/IRF3, xCT, FTH1, and GPX4 in hippocampal tissues from each group. J, Representative C11-BODIPY 581/591 fluorescence images of primary hippocampal neurons under normoxic, hypoxic, or hypoxic + C-176 conditions and quantification of the red/green fluorescence ratio. Body weight data were analyzed by two-way repeated-measures ANOVA followed by appropriate post hoc multiple comparisons; other comparisons were analyzed by one-way ANOVA followed by appropriate post hoc multiple comparisons. Brown–Forsythe and Bartlett tests were used to assess homogeneity of variances, and no unequal variances were indicated among groups. Behavioral experiments: n = 8 mice per group; molecular and cellular experiments: n = 4 independent biological replicates. ns, not significant; *P < 0.05, **P < 0.01, ***P < 0.001, ****P < 0.0001.

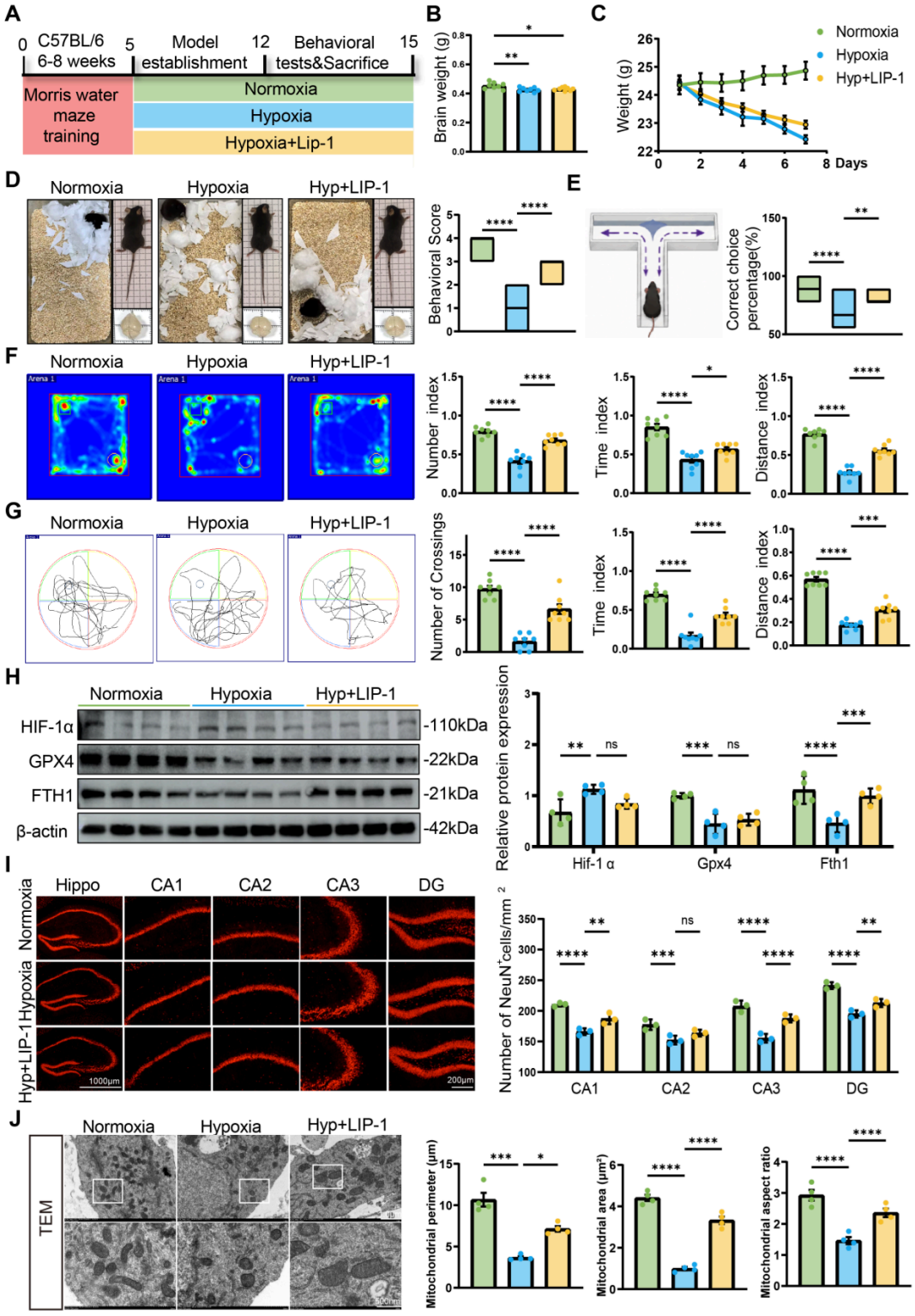


Figure 6

Liproxstatin-1 alleviates hypoxia-induced cognitive dysfunction and hippocampal neuronal injury.

A, Experimental scheme of intervention with the classical ferroptosis inhibitor Liproxstatin-1 (LIP-1) during hypoxia; LIP-1 was administered by intraperitoneal injection at 10 mg/kg once daily for 7 consecutive days. B, Quantification of brain weights in each group. C, Dynamic changes in body weight.

D, Representative images of the nest building test and behavioral scores. E, Correct choice rate in the T-maze test. F, Representative activity heatmaps of the NOR test and quantification of the exploration count, time, and distance indices. G, Representative swimming trajectories in the MWM spatial probe test and quantification of platform-site crossings, time index, and distance index. H, Representative Western blots and quantification of HIF-1α, GPX4, and FTH1 in hippocampal tissues. I, Representative NeuN immunofluorescence images of the hippocampus and its subregions CA1, CA2, CA3, and DG and quantification of NeuN-positive neurons. J, Representative TEM images of primary hippocampal neurons treated with normoxia, hypoxia, or hypoxia + LIP-1 and quantification of mitochondrial area, perimeter, and aspect ratio. Behavioral experiments: n = 8 mice per group; molecular and histological experiments: n = 3–4 independent biological samples per group. ns, not significant; *P < 0.05, **P < 0.01, ***P < 0.001, ****P < 0.0001.

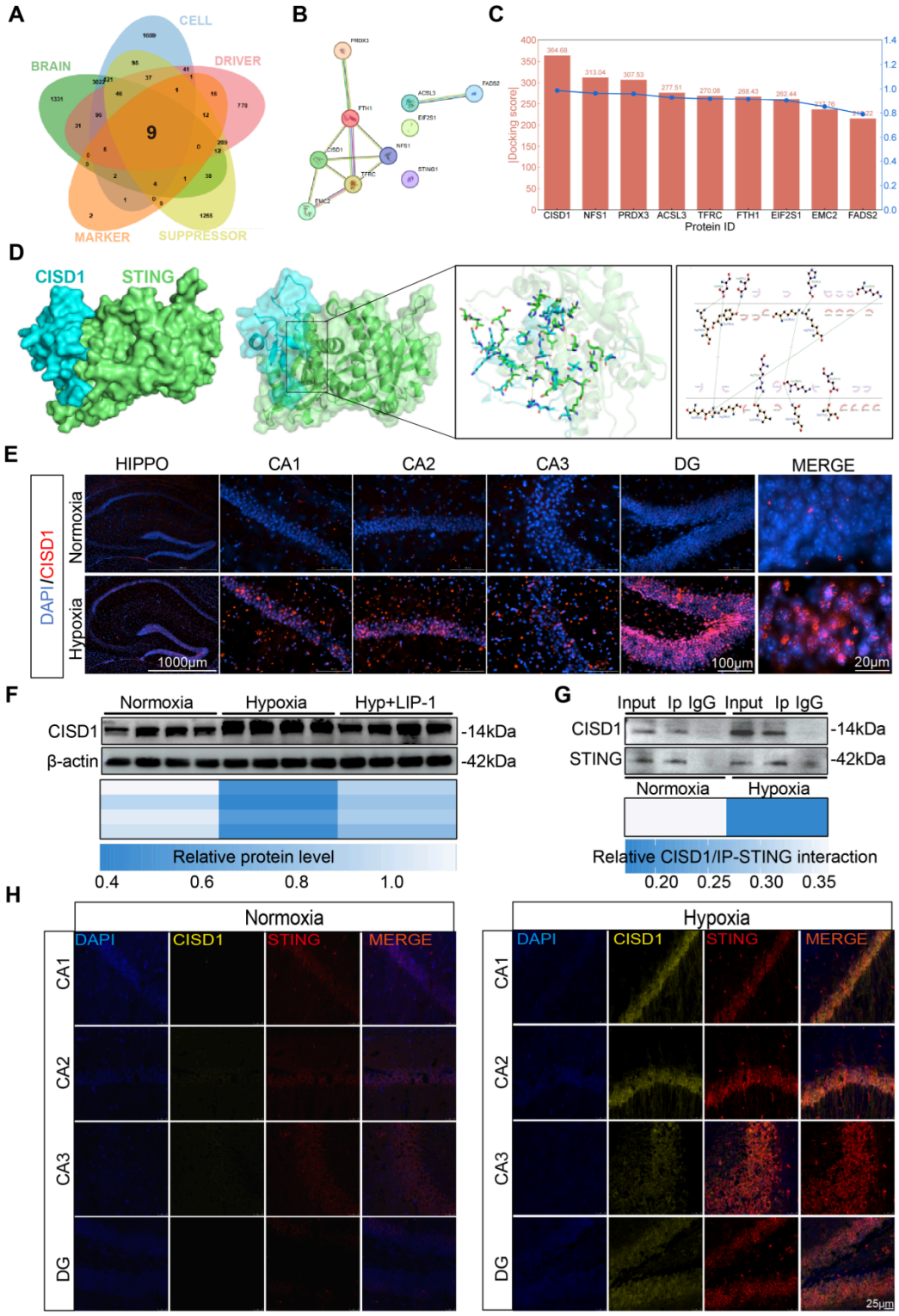


Figure 7

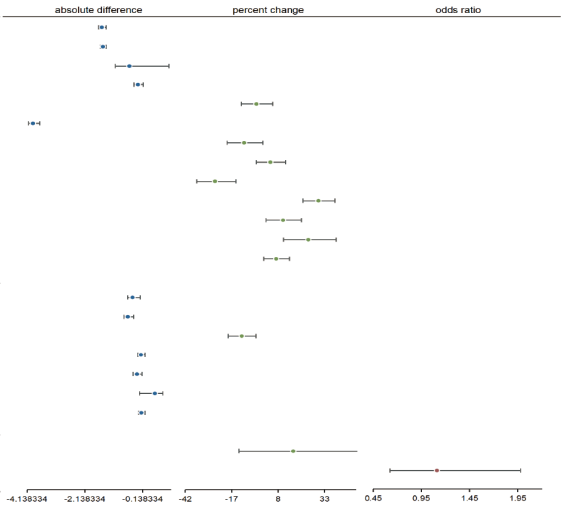
Hypoxia promotes the interaction between STING and the mitochondrial iron-sulfur protein CISD1.

A, Venn diagram of proteins identified by proteomic sequencing following immunoprecipitation with a STING-specific antibody from hypoxic hippocampal tissues and primary hippocampal neurons, intersected with a ferroptosis-related gene database, yielding 9 potential STING-ferroptosis-related

interacting proteins. B, Protein–protein interaction (PPI) network analysis of the 9 candidate proteins. C, Molecular docking scores of the candidate proteins with STING; the STING structure was derived from PDB: 4LOJ, and the CISD1 structure from AlphaFold: AF-Q91WS0-F1. D, Predicted three-dimensional binding conformation of CISD1 and STING, with magnified views of the binding interface and interacting residues. E, Representative CISD1 immunofluorescence images of the hippocampus and its subregions CA1, CA2, CA3, and DG in the normoxia, hypoxia, and hypoxia + LIP-1 groups. F, Representative Western blot and quantification of CISD1 protein in the hippocampus (n = 4). G, Co-immunoprecipitation (Co-IP) experiments and quantification of the STING–CISD1 interaction under normoxic/hypoxic conditions. H, Representative immunofluorescence co-staining images of CISD1 and STING in the hippocampus and its subregions CA1, CA2, CA3, and DG under normoxic and hypoxic conditions.

A

Indicator	<2500 m(n=123)	≥2500 m(n=187)	Statistic/effect	P value	FDR q
Baseline characteristics					
Age, years	17.99 ± 0.63	18.54 ± 0.75	SMD 0.79		
Male sex	Male 57/123 (46.0%)	Male 56/187 (29.9%)	SMD -0.33		
Height, cm	168.38 ± 8.07	163.24 ± 6.92	SMD -0.68		
Weight, kg	63.43 ± 11.82	54.90 ± 8.41	SMD -0.83		
BMI, kg/m²	22.32 ± 3.62	20.57 ± 2.65	SMD -0.55		
Liver function					
Total protein	71.54 ± 3.37	68.01 ± 3.17	β -2.76 (-3.56, -1.96)	<0.001	<0.001
Albumin	47.21 ± 2.59	44.11 ± 2.30	β -2.52 (-3.07, -1.98)	<0.001	<0.001
Globulin	24.33 ± 2.34	23.91 ± 2.66	β -0.24 (-0.88, 0.40)	0.467	0.489
Albumin/globulin ratio	1.96 ± 0.22	1.87 ± 0.24	β -0.08 (-0.14, -0.02)	0.006	0.012
Total bilirubin	15.16 [11.84, 19.07]	14.10 [10.82, 18.41]	-3.7% (-11.8, 5.2)	0.401	0.441
Cholinesterase	7911.27 ± 1498.20	6727.01 ± 1191.74	β -688.93 (-984.77, -393.09)	<0.001	<0.001
Indirect bilirubin	8.18 [5.89, 10.27]	6.93 [5.14, 9.62]	-10.3% (-19.5, -0.1)	0.048	0.066
Direct bilirubin	7.07 [5.72, 8.00]	7.20 [5.57, 8.80]	3.8% (-3.7, 12.0)	0.328	0.38
Total bile acid	3.22 [2.24, 4.79]	2.54 [1.75, 3.50]	-26.0% (-35.8, -14.7)	<0.001	<0.001
Alkaline phosphatase	92.53 [78.88, 110.85]	115.21 [96.67, 133.99]	29.7% (21.4, 38.6)	<0.001	<0.001
GGT	15.51 [12.79, 19.62]	15.20 [12.21, 20.06]	10.6% (1.6, 20.5)	0.02	0.032
ALT	15.50 [11.55, 23.40]	17.30 [13.55, 23.70]	24.3% (10.9, 39.3)	<0.001	<0.001
AST	20.85 [17.93, 24.30]	21.40 [19.01, 24.54]	6.9% (0.3, 14.1)	0.041	0.061
Lipids					
LDL-C	2.18 ± 0.52	1.92 ± 0.45	β -0.17 (-0.28, -0.05)	0.004	0.009
Total cholesterol	3.59 ± 0.59	3.25 ± 0.50	β -0.28 (-0.41, -0.14)	<0.001	<0.001
Triglycerides	0.64 [0.50, 0.79]	0.53 [0.45, 0.68]	-11.6% (-18.7, -3.9)	0.004	0.009
Apolipoprotein A1	1.28 ± 0.16	1.26 ± 0.13	β -0.05 (-0.08, -0.01)	0.008	0.014
HDL-C	1.36 ± 0.30	1.32 ± 0.21	β -0.09 (-0.15, -0.03)	0.003	0.007
Apolipoprotein A/B	2.15 ± 0.58	2.38 ± 0.53	β 0.07 (-0.06, 0.21)	0.275	0.356
Apolipoprotein B	0.63 ± 0.15	0.55 ± 0.12	β -0.04 (-0.07, -0.01)	0.008	0.014
Inflammation					
hs-CRP	0.47 [0.21, 1.14]	0.30 [0.17, 0.77]	16.2% (-13.2, 55.5)	0.313	0.38
IL-6 >2.5	>2.5: 38/124 (30.6%)	>2.5: 62/187 (33.2%)	OR 1.11 (0.63, 1.98)	0.719	0.719



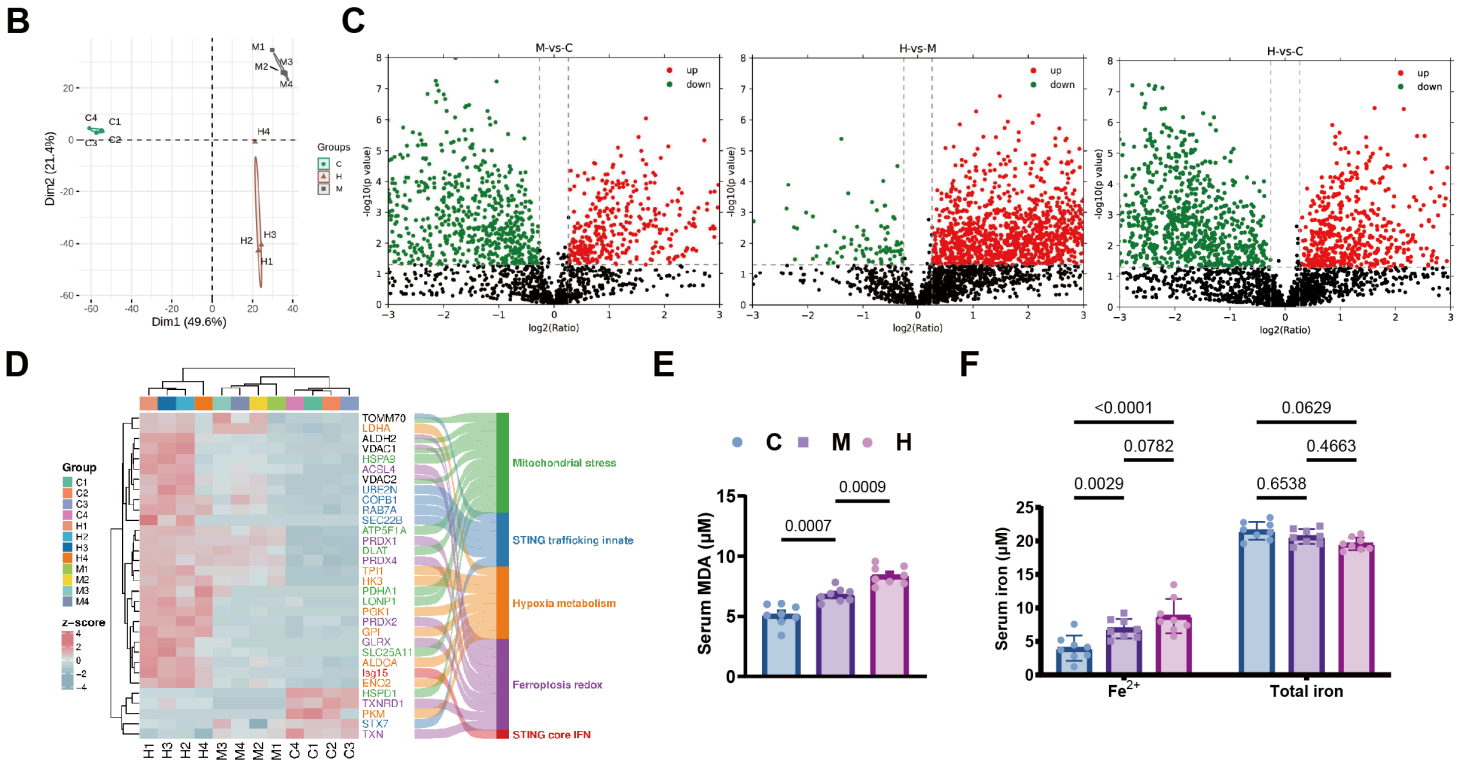


Figure 8

Systemic metabolic, inflammatory, and iron homeostasis alterations in individuals living at different altitudes.

A, Clinical and blood biochemical characteristics of the cohort stratified into two groups according to long-term residential altitude (using the international standard cutoff of 2500 m; n = 123 for <2500 m and n = 187 for ≥2500 m), with effect sizes and statistical comparisons shown. B, PCA of serum proteomics data after further subdivision into low-altitude (C), mid-altitude (M), and high-altitude (H)

groups (n = 4). C, Volcano plots of differentially expressed proteins in pairwise comparisons between altitude groups. D, Heatmap and functional/pathway annotation of altitude-related differentially expressed proteins. E, Serum MDA levels in the different altitude groups. F, Serum Fe^{2+} and total iron levels in the different altitude groups. For serum biochemical assays, n = 8 samples per group; comparisons among the three groups were performed by one-way ANOVA followed by appropriate post hoc multiple comparisons, and exact P values are indicated in the figure.

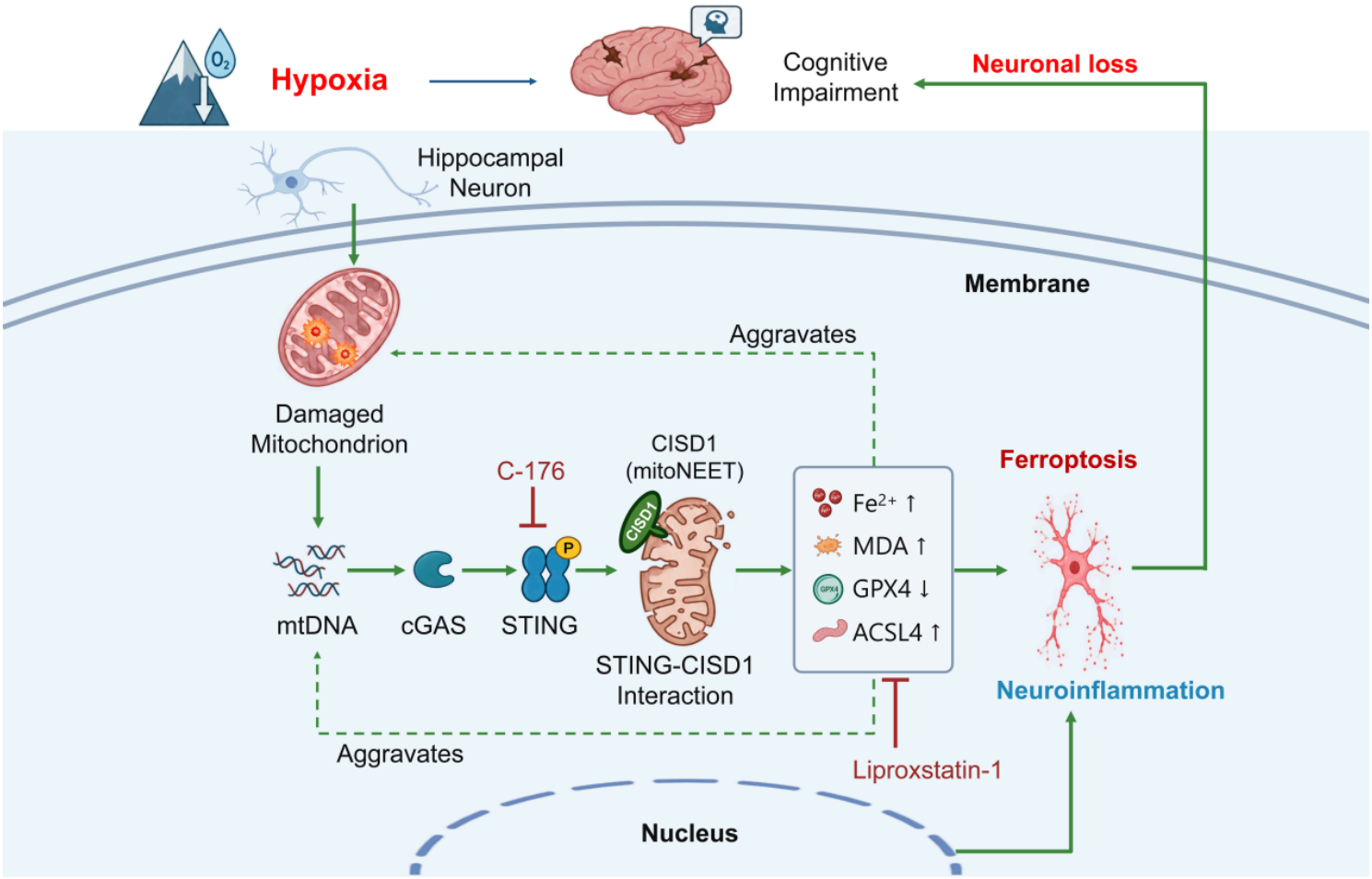


Figure 9

Working model: hypoxia drives hypoxic cognitive impairment via the mitochondrial damage–mtDNA–cGAS–STING–CISD1–ferroptosis axis.

Hypobaric hypoxia causes hippocampal mitochondrial damage and mtDNA release, activating cGAS–STING signaling. STING interacts with the mitochondrial outer membrane protein CISD1 (mitoNEET), driving neuronal ferroptosis (Fe^{2+} and MDA ↑, GPX4 ↓, ACSL4 ↑), neuronal loss, and cognitive impairment. Ferroptosis in turn aggravates mitochondrial damage, forming a self-amplifying feed-forward loop. C-176 blocks STING activation, whereas Liproxstatin-1 suppresses ferroptosis downstream; both interventions alleviate neuronal loss and cognitive impairment.

Supplementary Files

This is a list of supplementary files associated with this preprint. Click to download.

- Supplementaryinformation.pdf